Ocean Modelling 43–44 (2012) 77–93

Contents lists available at SciVerse ScienceDirect

Ocean Modelling

journal homepage: www.elsevier.com/locate/ocemod

Large-scale impacts of submesoscale dynamics on phytoplankton: Local and remote effects

M. Lévy [a,*], D. Iovino [a], L. Resplandy [a], P. Klein [b], G. Madec [a], A.-M. Tréguier [b], S. Masson [a], K. Takahashi [c]

[a] LOCEAN-IPSL, CNRS/UPMC/IRD/MNHN, Paris, France
[b] LPO, CNRS/IFREMER/IRD/UBO, Brest, France
[c] ESC, Yokohama, Japan

ARTICLE INFO

Article history:
Received 11 April 2011
Received in revised form 29 November 2011
Accepted 6 December 2011
Available online 30 December 2011

Keywords:
Submesoscale
Large-scale
Phytoplankton
Primary production
Grazing
Nutricline
Thermocline

ABSTRACT

The sensitivity of an idealized bio-physical model of seasonally varying subtropical and subpolar gyres to increased horizontal resolution is presented. Switching from mesoscale-resolving (1/9°) to submesoscale-resolving (1/54°) allows the emergence of a denser and more energetic vortex population sustained by submesoscale physics. The experiments display a global decrease in phytoplankton abundance of ~10–20% as the resolution is refined. This result contrasts with previous studies, which suggested that eddy-driven vertical fluxes of nutrients *locally* boost phytoplankton growth at mid-latitudes in the open ocean. The explanation is that the long-term (50 years) modification of the large-scale, or basin-scale, circulation and distribution of nutrients by submesoscale processes (*remote* effects), not taken into account by previous studies because of their much shorter time integration, balance the *local*, small-scale effects. More precisely, *dynamical remote* effects (involving only the physics) affect the location of the boundary between the two gyres as well as the large-scale mixed-layer depth (MLD) and thermocline depth. *Biological remote* effects result from the *dynamical remote* effects that strongly modify the physical–biological interactions at all scales, including at large scales. These *biological remote* effects involve changes of the nutricline depth. In the mid-latitude subpolar gyre, phytoplankton decrease in abundance at higher resolution is due to the shallower MLD and nutricline, which promote zooplankton grazing; in the subtropical gyre, it is due to deeper MLD and nutricline, which diminishes regenerated production. In addition, *remote* effects modulate the dynamical supplies of nutrients to the euphotic layer through a combination of changes in mean advection, eddy advection and vertical mixing.

1. Introduction

Satellite ocean color climatologies reveal large contrasts in sea surface phytoplankton distribution at the scale of oceanic basins, with maxima over upwelling regions, such as the subpolar gyres and tropics, reducing to lower values over the flanks of subtropical gyres and with marked minima in the center of subtropical gyres (Feldmann et al., 1989). These large-scale contrasts primarily result from the large-scale upwelling and downwelling of growth-limiting nutrients induced by the wind forced circulation, and are captured by coarse resolution Biogeochemical Ocean General Circulation Models (Bio-OGCM). They go together with a marked seasonality at mid and high latitudes, driven by the seasonal changes in insolation and in mixed-layer depth (MLD). However, this large-scale seasonal view only depicts the average of a reality that presents a great deal of variability in a large spatial range including large and submesoscales. In particular, the submesoscale variability associated with the oceanic turbulence is ubiquitous on instantaneous, synoptic ocean color images, and has an amplitude that can reach that of the large-scale contrasts over a few kilometers to tens of kilometers (Gower et al., 1980).

High-resolution observations of ocean color have raised the question of the importance of this small-scale variability on the large-scale budget of phytoplankton. In regions where phytoplankton production balances nutrient supplies to the euphotic zone, one key question is how submesoscale nutrient injection compares with the large-scale, convective and wind forced supplies. Another question is how submesoscale processes affect the functioning of the biogeochemical system as a whole, including new production, regeneration and grazing, and ultimately controls the abundance of phytoplankton.

The submesoscale variability, with scales as small as $\mathcal{O}(10)$ km, falls below the grid size of current Bio-OGCMs. Today, the most powerful supercomputers allow the first global simulations of the ocean circulation at (1/10)° (Maltrud and McClean, 2005; Nakamura and Kagimoto, 2006; Sasaki et al., 2008; Le-Galloudec

* Corresponding author. Tel.: +33 1 44 27 27 07.
E-mail addresses: marina@locean-ipsl.upmc.fr, marina.levy@upmc.fr (M. Lévy).

1463-5003/$ - see front matter © 2011 Elsevier Ltd. All rights reserved.
doi:10.1016/j.ocemod.2011.12.003

et al., 2008). These experiments are eddy-resolving, but not submesoscale resolving. Moving from mesoscale to submesoscale resolution in bio-physical models requires an increase in computer power of approximately two orders of magnitude. This is still out of reach for modeling the global ocean, but is technically feasible over oceanic domains of limited extent.

The present study aims at examining the consequences of explicit resolution of submesoscale features on the basin-scale budget of primary production and phytoplankton abundance in a bio-physical ocean model. The large-scale context considered is a mean seasonal cycle in a closed basin representative of the western sector of the North Atlantic or North Pacific, including a subtropical and a subpolar gyre. The experimental protocol is chosen to highlight the large-scale changes in phytoplankton abundance and productivity resulting from an increase in horizontal resolution from eddy-resolving (1/9°) to submesoscale resolving (1/54°). In order to provide a consistent picture of how submesoscale turbulence impacts phytoplankton, we conduct experiments long enough (50 years) to account for the feedbacks of submesoscale physics on the large-scale circulation and on the large-scale distribution of tracers, in particular of the long-lived pools, i.e. nitrate and dissolved organic matter (DOM) in the top 500 m, which ultimately feed primary production. This contrasts with previous studies that focused on the impact of submesoscale processes over short space (a few 100 km) and time (a few months) scales.

In a previous paper (Lévy et al., 2010), we have examined the changes in the basin-scale circulation and pattern of the ventilated thermocline when switching from (1/9)° to (1/54)°. These large-scale changes entirely result from the submesoscale dynamics being explicitly solved at (1/54)° but not at (1/9)°. We refer to them as the *dynamical remote* effects of submesoscale dynamics because they involve global changes which are non-local in space and time. Here, we focus on the large-scale changes in the distribution of nutrients and in the production and loss of phytoplankton resulting from the submesoscale dynamics. We call them *biological remote* effects. We show that these effects are driven by the *dynamical remote* effects that modify the physical-biological interactions at all scales including large scales. We examine how these effects lead to different large-scale distributions of nutrients and phytoplankton in the two simulations. These large-scale changes are observed after tens of years when the basin-scale circulation is equilibrated, i.e. on a significantly much longer time than the time-scale of submesoscale processes (a few days). In contrast, the *local effect* of submesoscale dynamics is defined as resulting from the physical–biological interactions at small-scale. These concepts of *remote and local effects* are developed in the next section. Then, the simulations are described and the changes in the physics highlighted in Lévy et al. (2010) are summarized in Sections 3 and 4, respectively. The responses of the biogeochemical system, in terms of nutrient distribution, phytoplankton production and planktonic abundance are presented and interpreted in Sections 5–7. Finally, the main results are highlighted and discussed in the last section.

2. Introducing the concepts of local and remote effects

2.1. Previous understanding of the impact of submesoscale dynamics: local effects

The *local* impacts of mesoscale turbulence on phytoplankton production are now widely recognized (see Lévy (2008) for a review). There is growing evidence that nutrient supplies occurring at the scale of eddies (the mesoscale) and at the scale of frontogenesis (the submesoscale) contribute significantly to the primary production budget. Models and observations both demonstrate that as spatial sampling resolution increases, so do the measured strength and variability of the vertical motions in the ocean (Pollard and Regier, 1990; Allen et al., 2001; Thomas et al., 2007; Thomas and Ferrari, 2008; Capet et al., 2008; Klein et al., 2008; Klein and Lapeyre, 2009; Thomas et al., 2010). These submesoscale vertical motions, driven by strongly nonlinear dynamics (Mahadevan and Tandon, 2006), can have profound effects on the local structure and dynamics of the planktonic ecosystem (Martin et al., 2001; Allen et al., 2005; Rivière and Pondaven, 2006; Viúdez and Claret, 2009; Perruche et al., 2011; Calil and Richards, 2010), and on the carbon (Omta et al., 2007) and nutrient fluxes through the system (Lévy et al., 2001b; Lévy et al., 2009; Martin and Pondaven, 2003; McGillicuddy et al., 2007; Nagai et al., 2008; Johnson et al., 2010).

Different aspects of the *local* impacts of mesoscale turbulence on primary production have been examined in some of our previous model studies. These studies have examined how specific processes perturb the system on the short term, through high-resolution ($\mathcal{O}(1)$ km in the horizontal) process-oriented model simulations. To recall some of the main results, a first set of experiments focused on vertical movement and transport. In Lévy et al. (2001b), the biogeochemical consequences of intense vertical velocities at submesoscale fronts, in phase with the vorticity gradients, were examined. It was shown that these vertical velocities can provoke the development of phytoplankton in filaments of negative vorticity, partly balanced by an export of phytoplankton in filaments of positive vorticity. These results have suggested that the net balance is toward a significant increase of primary production when submesoscale vertical velocities are energetic, but similar simulations with quasi-geostrophic mesoscale vertical velocities led to a more moderate increase (Lévy and Klein, 2004). In contrast, a coastal study showed that in the presence of large-scale upwelling, the main impact of submesoscale turbulence was the subduction of phytoplankton (Lathuiliere et al., 2011; Lathuilière et al., 2010). A second set of experiments focused on the stratification of the surface mixed-layer by submesoscale dynamics (Lévy et al., 1998; Lévy et al., 2005; Karleskind et al., 2011a,b): in such cases, the mixed-layer shoaling in specific submesoscale features provokes the bloom to begin prior to seasonal stratification.

2.2. A more complete view: accounting for remote effects

Up to now, quantification of the impact of submesoscale dynamics was based on numerical experiments integrated over relatively short periods of time (typically 1 year or less) leaving the mean (large-scale) circulation unchanged. However, a complete picture of the impact of submesoscale turbulence on phytoplankton has to account not only for the *local*, short-term impact, but also for how, on the long-term, these short term and local processes feedback on large-scale quantities.

Submesoscale resolving numerical experiments show significant deviation from eddy-resolving experiments, in particular an increase in the number of eddies (Hurlburt and Hogan, 2000; Siegel et al., 2001; Klein et al., 2008; Lévy et al., 2010). This highlights the crucial role of submesoscale physics in sustaining an energetic mesoscale circulation, because mesoscale eddies are surrounded by strong submesoscale vorticity gradients that act as dynamical barriers. These transport barriers re-inforce the eddies, making them more coherent and longer-lived. In turn, the stronger mesoscale activity plays an active role in the large-scale circulation (Gent and McWilliams, 1990; Gent et al., 1995). This feedback of the submesoscale on the mesoscale, and of the mesoscale on the large scale occurs through the non-linear terms in the primitive equations and is the manifestation of the inverse cascade which is characteristic of rotating turbulent fluids. The contribution of submesoscale processes to the mean dynamical fields involves the positioning and strengthening of jets, and, through the thermal

wind balance, the global equilibration of the thermocline. It is thus non local in space and time. We refer to this feedback as the *dynamical remote* effect of submesoscale processes.

Submesoscale processes are likely to affect marine biogeochemical cycles not only through submesoscale nutrient fluxes but also through their *dynamical remote* effects. Ultimately, the *remote* effects modify the bio-physical interactions at all scales including large-scales. This leads to significant impact on the large-scale equilibrium of the nutrient distribution, i.e. on the subsurface nitrate reservoir and on the distribution of DOM (which is the main source of ammonium). This *biogeochemical remote* effect of eddies is still unknown to a large extent. It is essential because it ultimately controls the availability of nutrients, which are necessary for phytoplankton growth. What are the long-term processes that affect the distribution of nitrate and DOM? In the 1D view, the upward flux of nutrients into the euphotic layer is balanced locally by a downward flux of organic material, which is then slowly remineralized at depth. In the 3D view, the lateral processes that deliver nutrients must also be considered in the balance. These lateral processes include the large-scale Ekman transport (Williams and Follows, 1998), the transport by large-scale currents (Krémeur et al., 2009), the eddy transport (Lee and Williams, 2000), and the transport by submesoscale structures (d'Ovidio et al., 2009; Lehahn et al., 2007; Haza et al., 2008; Waugh and Abraham, 2008; LeSommer et al., 2011).

2.3. Reynolds decomposition

The *remote/local* concepts can be rationalized by separating any field F (F being a tracer concentration or velocity field) into a mean large-scale component $\overline{F}$ and small-scale departure from the mean F' ($F = \overline{F} + F'$ with $\overline{F'} = 0$). So far, the question of the impact of mesoscale and submesoscale dynamics on biogeochemistry has essentially addressed how perturbations of the circulation (V') were affecting the distribution and growth of the mean phytoplankton concentration $\overline{P}$, given a mean nutrient distribution $\overline{N}$. In this approach, the local impacts of submesoscale features enter the nutrient and phytoplankton evolution equation through the non-linear Reynolds terms which involve cross products of N', P' and V' (Lévy, 2008). However, a complete estimate of the impact of submesoscale processes has also to account for the feedback of submesoscale processes on the large-scale quantities $\overline{V}$ and $\overline{N}$. In this work, conducting long experiments allows us to account for this feedback.

In practice, we conduct two experiments with different grid resolution and compare the annual mean distributions after a spin-up of 50 years. The comparison of the two annual means, one obtained with explicit resolution of submesoscales, and the other without, illustrates the total impact of submesoscale dynamics, including *remote* and *local* effects. In Section 7, we go one step further and analyze the contributions of the mean and eddy advective terms in the nitrate equation for the two experiments. The difference in the mean terms reflects the *remote* impacts, and the difference in the eddy terms reflect the *local* impact, although the eddy terms are also affected by the changes in the mean fields.

3. Model experiments and equilibration

The setting is a double-gyre, meant to represent an idealized western sector of the North Atlantic or North Pacific ocean. The domain geometry is a closed rectangular basin on the β-plane centered at 30°N and rotated by 45°, 3180 km long, 2120 km wide and with a constant depth of 4000 m. The circulation is forced by analytical profiles of wind, solar radiation, heat and salt fluxes, which vary seasonally and zonally as shown in Fig. 1.

Two simulations are performed with different horizontal resolution and, accordingly, lateral sub-grid scale closures (Table 1). The resolution of B9 ($\sim$1/9°) is comparable to that of state of the art global eddy-resolving ocean models (Sasaki et al., 2008; Maltrud and McClean, 2005; Le-Galloudec et al., 2008). The resolution of B9 has been increased to the resolution of B54 ($\sim$ 1/54°) by dividing each cell equally into 6×6. In both experiments, there are 30 z-coordinate vertical layers, whose thicknesses vary from 10 to 20 m in the upper 100 m, and increase up to 300 m at the bottom.

Bi-harmonic friction and bi-harmonic diffusion along horizontal surfaces are used (Table 1). Vertical mixing is parameterized by a turbulent closure model (Blanke and Delecluse, 1993), with a background value of 10^{-5} m^2 s^{-1}. Vertical mixing coefficients are enhanced to 100 m^2 s^{-1} in the case of convection. Advection of temperature, salinity and biogeochemical tracers is performed with a flux-corrected transport scheme (Lévy et al., 2001a). An energy conserving scheme is used for the computation of vorticity trends (Madec, 2008). Free-slip conditions and no heat and salt flux are applied along solid boundaries, except at the bottom where a non-linear friction drag is applied. The NEMO primitive equation ocean model is used, in its level-coordinate, free-surface version (Madec, 2008).

The LOBSTER biogeochemical model (Tables 2 and 3) is embedded within the physical model. It solves the evolution of six biogeochemical variables: phytoplankton, zooplankton, detritus, semi-labile DOM, nitrate and ammonium. The model solves for the uptake of nitrate by phytoplankton, the uptake of ammonium by phytoplankton, grazing of phytoplankton by zooplankton, and a simplified remineralization network, which involves excretion by zooplankton, dissolution of detritus, accumulation of semi-labile DOM, remineralization of DOM into ammonium, and ultimately, nitrification of ammonium into nitrate. The biogeochemical model is fully tracer conserving and does not include any restoring to nutrient profiles below the euphotic zone (as has been applied in some earlier studies, i.e. Mc Gillucuddy et al., 2003). The same set of equations is applied throughout the entire water column. Primary production is computed as the sum of nitrate and ammonium uptakes by phytoplankton. Production is presented as a depth-integral over the euphotic layer, which we approximated by the layer extending from the surface down to 120 m depth. The choice of a fixed layer for the euphotic zone facilitated the comparison between the two experiments.

The experiments start after a spin-up of 850 years at low resolution (1°, B1). B1 is initialized at rest with vertical profiles of temperature, salinity and biogeochemical tracers uniformly applied to the whole domain. The temperature, salinity and nitrate initial profiles were constructed from the World Ocean Atlas climatologies by averaging over 25–30°N and 80–0°W. The profiles were truncated to constant values below 1000 m which allowed equilibration of the deep waters (which are not of interest here) in B1 after only 850 years of integration.

The initial profiles of the other biogeochemical variables were initially set to low values. After 850 years of simulation, B1 is at equilibrium: a two gyre structure is formed, with a depressed nitracline and oligotrophic regime in the subtropical gyre and a raised nutricline and eutrophic regime in the subpolar gyre. B9 and B54 are initialized from the spun-up state of B1 and run for another 50 years to adjust the basin with the new resolutions (Fig. 2). The change of resolution induces changes in circulation which co-occur with modification of the thermohaline structure that builds up during the 50-year spin-up. After 50 years of integration, the two experiments reach a state which is close to equilibrium in the upper 500 meters (Fig. 2). At this point, an additional 5-year run is conducted with outputs averaged over two days. The model "mean state" is shown in this work as an

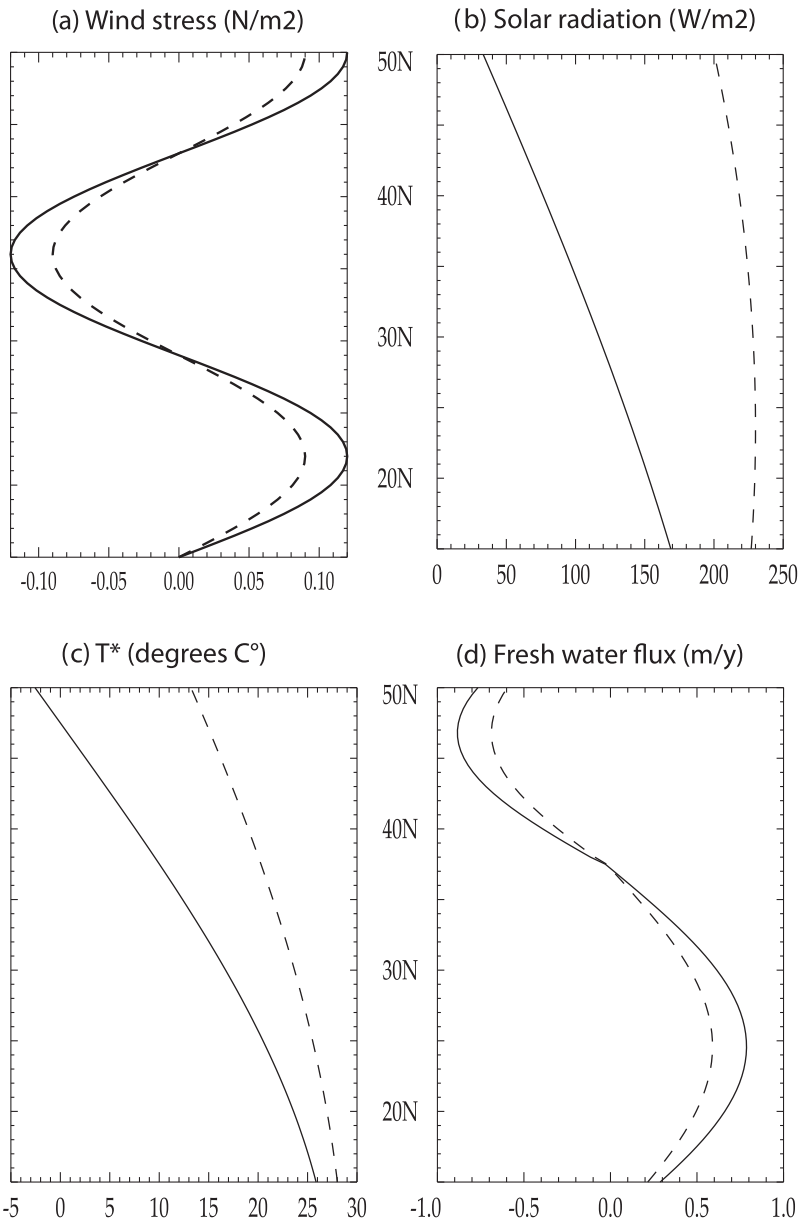

Fig. 1. Atmospheric forcings of the model as function of latitude. (a) Wind stress, (b) Penetrative solar radiation, (c) Apparent temperature and (d) Fresh water flux. The forcings vary between winter (solid line) and summer (dashed line) extrema in a sinusoidal manner. The net heat flux is parametrized as a restoration toward the apparent temperature.

annual quantity computed by averaging the last 5 years of model results.

The choice of this idealized geometry is motivated by the studies of Drijfhout (1994), Hazeleger et al. (1996) and Hazeleger and Drijfhout (1999, 2000a,b) which showed that it could capture the basic features of the North Atlantic circulation in a domain with a reduced size, thus allowing for faster equilibration than in a more realistic setting. The model mean state results from the full equilibration of momentum and tracers over the domain geometry, given the model forcing fields. It presents similarities with the real ocean because of the similarity in the forcing. However, the model domain is much smaller than the Atlantic or Pacific basins, and both topographic effects and the contribution of water mass formation in marginal seas are not accounted for. For these reasons, the equilibrated distributions of temperature, salinity or nitrate cannot be compared directly with existing observations from the real ocean although they capture dominant features of the North Pacific or the North Atlantic. In particular, the mean seasonality in our model subtropical and subpolar gyres is reasonable when compared to the observed seasonality in the North Atlantic (see Krémeur et al. (2009), auxiliary material). The dynamical aspects of the high-resolution simulations have been previously analyzed in Lévy et al. (2010). The mean features of the biological system in a earlier model version at 1/3° were presented in Krémeur et al. (2009).

4. Impact of submesoscale processes on the gyre circulation

This section summarizes the differences in ocean dynamics that emerge when switching from (1/9)° to (1/54)° (Lévy et al., 2010), with a focus on the parameters that are particularly relevant for phytoplankton.

Table 1
Parameters and important features of the model experiments. All computations are performed on the Earth Simulator at Yokohama, Japan. Real computing time is the total computing time for the 50 years of spin-up. The terms K_M and K_T are the eddy viscosity and eddy diffusivity coefficients, respectively. The slope of the velocity spectra is computed between wave numbers k = 30 and k = 70. EKE is the domain-mean surface eddy kinetic energy. W2 is the domain-mean 0–500m vertical velocity variance.

	B9	B54
Horizontal resolution	11.8 km	2.0 km
Horizontal grid points	180×270	1080×1620
Time step	20 mn	2 mn
Number of processors	7	216
Real computing time (hour)	400	120 000
K_M	-5×10^{10} m^4 s^{-1}	-10^9 m^4 s^{-1}
K_T	-10^9 m^4 s^{-1}	-10^9 m^4 s^{-1}
Vorticity maximum (units of f)	1.5	4
Skewness	1	2
Slope of velocity spectra	−3.0	−1.9
EKE (10^{-4} m^2 s^{-2})	199	312
W2 (m^2 d^{-2})	13.3	17.4

4.1. Mesoscale turbulence

The most visible impact of increasing the resolution is the emergence of smaller eddies and filamentary structures resulting from the non-linear interactions between eddies (Fig. 3a,b). In B9, wave-like undulations are evident on the western side of the domain, between 30–35°, which is where the western boundary current extends eastward (Fig. 4b). These instabilities occasionally lead to the formation of large eddies (200 km diameter), essentially close to the western boundary where the jet is the most intense. With increased resolution, more coherent axisymmetric eddies begin to emerge leading to a denser and well defined vortex population, covering a wide range of scales. The eddies have diameters between 50 and 200 km. Some are well separated from the jet, others are rapidly re-absorbed into the jet. Dipole vortices and submesoscale filaments are also present.

Because eddies are mostly generated through baroclinic instability of the mean flow, the spatial distribution of eddies and filaments is highly heterogeneous (Fig. 3a,b). In B9, the area of high eddy activity is restricted to the offshore extension of the western boundary current (between $30-35°N$). In B54, it penetrates

Table 2
LOBSTER Model equations. The same set of equation is applied over the entire water column. A model for light absorption (Lévy et al., 2001) is used to compute the Photosynthetic available radiation (PAR) at each depth, as a function of the phytoplankton vertical profile and of the incoming solar radiation.

Description	Equation	
Nitrate source/sink	$S(NO_3) = -\mu_p L_l L_{NO_3} P + \mu_n NH_4 + \partial_z f$	(1)
Ammonium source/sink	$S(NH_4) = -\mu_p L_l L_{NH_4} P - \mu_n NH_4 + f_n(\gamma \mu_p L_l (L_{NO_3} + L_{NH_4})P + \mu_z Z + \mu_d D) + \mu_{dom} DOM$	(2)
Phytoplankton source/sink	$S(P) = (1-\gamma)\mu_p L_l (L_{NO_3} + L_{NH_4})P - G_p - m_p P$	(3)
Zooplankton source/sink	$S(Z) = a_z(G_p + G_d) - m_z Z^2 - \mu_z Z$	(4)
Detritus source/sink	$S(D) = (1-a_z)(G_p + G_d) + m_p P + f_z m_z Z^2 - G_d - \mu_d D - V_d \partial_z D$	(5)
DOM source/sink	$S(DOM) = (1-f_n)(\gamma \mu_p L_l (L_{NO_3} + L_{NH_4})P + \mu_z Z + \mu_d D) - \mu_{dom} DOM$	(6)
Light limitation	$L_l = 1 - e^{-\frac{PAR}{K_{par}}}$	(7)
Nitrate limitation	$L_{NO_3} = \frac{NO_3}{NO_3 + K_{no_3}} e^{-\psi NH_4}$	(8)
Ammonium limitation	$L_{NH_4} = \frac{NH_4}{NH_4 + K_{nh_4}}$	(9)
Grazing of phytoplankton	$G_p = g_z \frac{pP}{K_z + pP + (1-p)D} Z$	(10)
Grazing of detritus	$G_p = g_z \frac{(1-p)D}{K_z + pP + (1-p)D} Z$	(11)
Preference for phytoplankton	$p = \frac{\tilde{p}P}{(\tilde{p}P + (1-\tilde{p})D}$	(12)
Closure terms	$f(z_{bio}) = \int_0^{z_{bio}} (1-f_z) m_z Z^2 dz$	(13)
	$f(z) = f(z_{bio}) \left(\frac{z}{z_{bio}}\right)^{-0.858}$	(14)

Table 3
LOBSTER model parameters.

Parameter name	Symbol	Value	unit
Nitrate limitation half-saturation value	K_{no_3}	0.7	mmol m^{-3}
Ammonium limitation half-saturation value	K_{nh_4}	0.001	mmol m^{-3}
Inhibition of nitrate uptake by ammonium	ψ	3	
Light limitation half-saturation value	K_{par}	33.	Wm^{-2}
Phytoplankton maximal growth rate	μ_p	1.	d^{-1}
Phytoplankton exsudation rate	γ	0.05	
Phytoplankton mortality rate	m_p	0.05	d^{-1}
Grazing half-saturation value	K_z	1	mmol m^{-3}
Zooplankton maximal grazing rate	g_z	0.8	d^{-1}
Assimilated food fraction by zooplankton	a_z	0.7	
Zooplankton excretion rate	μ_z	0.07	d^{-1}
Zooplankton mortality rate	m_z	0.12	d^{-1} mmol^{-1} m^3
Zooplankton food preference	p	0.8	
Fraction of slow sinking mortality	f_z	0.5	
Nitrification rate	μ_n	0.05	d^{-1}
DOM breakdown rate	μ_{dom}	0.006	d^{-1}
Ammonium/DOM redistribution ratio	f_n	0.75	
Detritus sedimentation speed	V_d	3	m d^{-1}
Detritus remineralization rate	μ_d	0.05	d^{-1}

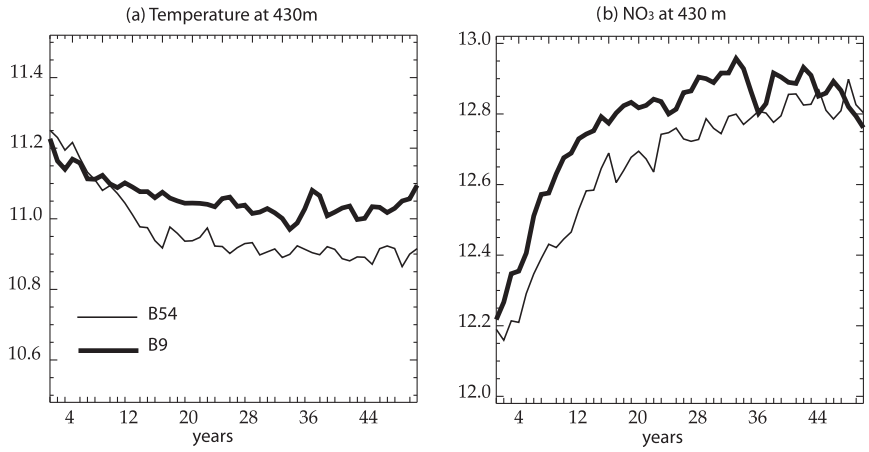

Fig. 2. Domain-averaged temperature (in °C) and nitrate concentration (in mmolNm^{-3}) at 430 m depth during the 50-year spin-up phase for experiments B9 and B54.

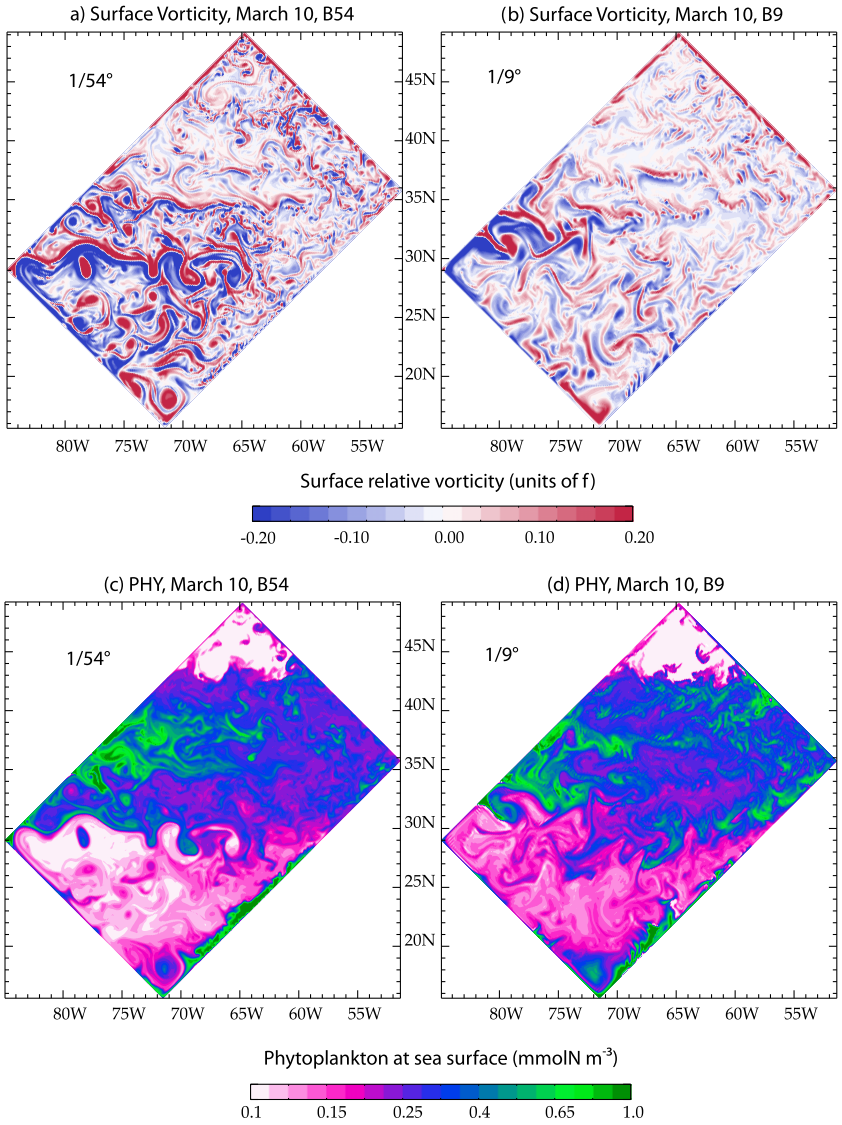

Fig. 3. (a and b) Relative vorticity at the surface on March 10. The color intervals are chosen to highlight the structures, but are not representative of the extremum values (see Table 1). (c and d) Phytoplankton concentration at the sea surface on March 10.

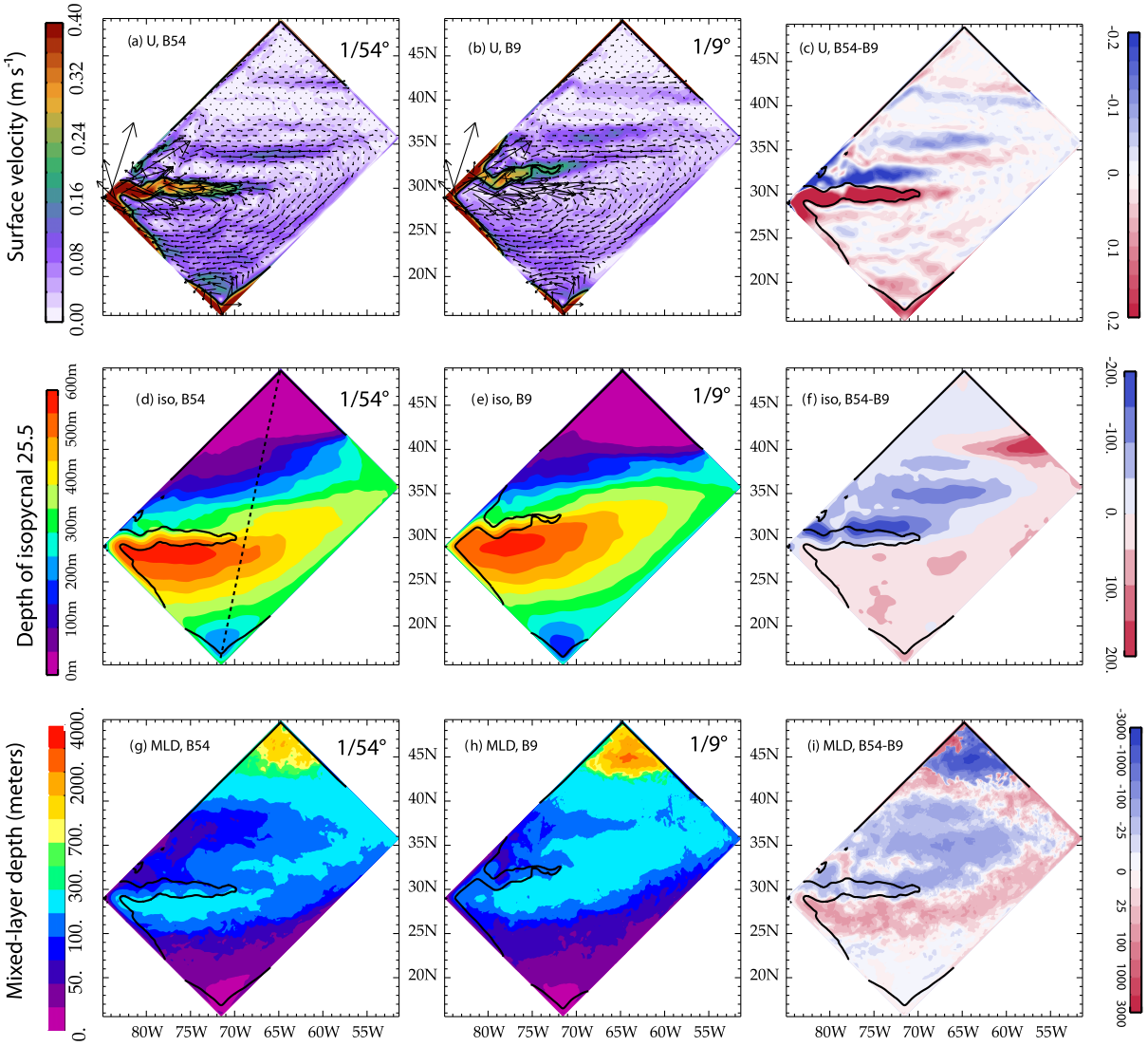

Fig. 4. Annual velocity in the euphotic layer (U), depth of the thermocline (iso) and winter mixed-layer depth (MLD). The first column shows the results for experiment B54, the second for B9 and the third is the difference between the two. The thermocline is defined as the depth of isopycnal 25.5. The MLD is computed as the interface of the surface layer whose density does not exceed the surface density by more than 0.01. The black contours overlaid on all figures indicates where horizontal velocity is larger than 0.2 ms^{-1}. The dotted line in (d) indicates the section shown in Fig. 5.

further westward and southward within the subtropical gyre, and an area of moderate eddy activity also develops in the north (on the western flank of the subpolar gyre). More statistical comparisons of the mesoscale turbulence in the two simulations, such as the slope of the velocity spectra and the skewness, are provided in Table 1. They confirm the importance of resolving the submesoscales even if these small scales are much less energetic. In agreement with previous studies (McWilliams, 1984; Provenzale, 1999), submesoscale resolution allows the simulation of stronger vorticity gradients, associated with stronger Reynolds stresses, which act as dynamical barriers and strongly reinforce the mesoscale activity. This is seen by the domain-averaged eddy kinetic energy which is increased by more than 50% between the two experiments (Table 1).

4.2. Ocean mean state

We now examine how the increased mesoscale and submesoscale dynamics in B54 globally impacts on the mean fields. In both experiments, the wind forces a counter clockwise subpolar gyre in the north and a clockwise subtropical gyre in the south, separated by a jet (Fig. 4a and b). This main mean jet is the offshore extension of the western boundary current and represents the model equivalent of the Gulf Stream or Kuroshio.

An essential difference between the two experiments lies in the separation latitude and extension of the main jet (Fig. 4c). Submesoscale processes make the separation latitude of the main jet to shift to the South and its offshore extension to penetrate further and more zonally to the east. This result ensues from the amplification of the impact of mesoscale turbulence on the western boundary current by submesoscale dynamics. This impact is known to affect both the jet separation latitude (Chassignet and Marshall, 2008) and its offshore extension (Barnier et al., 1991). It is noteworthy that, in both experiments, the jet is located a few degrees south of the theoretical boundary between the two gyres (forced at $\sim 36°N$ by the change of sign of the wind stress curl, Fig. 1). This southward shift is consistent with observations in the real ocean; for instance, the Kuroshio extension is located at about $35°N$, i.e. 7° south of the separation predicted by the linear theory ($43°N$).

Another important large-scale feedback of the stronger and more numerous eddies in B54 is the intensification of the mean currents. This intensification concerns the main jet discussed above, and also mean zonal jets that have directions alternating with latitude and speeds of several centimeters per second (Fig. 4a). These alternating zonal jets are present both in B54 and in B9, although in B9 they are less zonal and located at different latitudes (Fig. 4b). For instance, a secondary surface intensified eastward jet is found at 34°*N* in B54 and at 36°*N* in B9. Alternating zonal jets are ubiquitous features in the world oceans and have been observed in the time-averaged anomalies of the geostrophic velocities (Maximenko et al., 2005) as well as in situ (Memery et al., 2000). There is a consensus on the fact that mesoscale eddies play a central role in supporting these jets (Kamenkovich et al., 2009). Our results confirm that the jets emerge when mesoscale turbulence is well established, and that they get more numerous and more intense when turbulence is more energetic (Lévy et al., 2011).

The two-gyre structure is apparent in the density field with the subtropical gyre involving lighter waters (and thus a deeper thermocline) than the subpolar gyre (Fig. 4d,e and Fig. 5a,b). For simplicity, the thermocline is identified by the annual-mean depth of isopycnal 25.5 (Fig. 5a,b). In accordance with the thermal wind balance, the strengthening of the jet in B54, with respect to B9, is associated with the steepening of the isopycnal slopes. In addition, deeper isopycnals in the subtropical gyre and shallower isopycnals in the subpolar gyre are associated with a southward shift of the bowl shape. This shift is associated with the jet separation latitude that goes south from B9 to B54. (Fig. 4d,e and Fig. 5a,b). These changes imply a deeper thermocline in B54 south of 30°*N* (by ∼50 m), and on the contrary a shallower thermocline in a large western tongue-shaped region between 30 – 40°*N* (Fig. 4f). The difference in thermocline depth between the two experiments also reflects the changes in the zonality of the surface circulation (Fig. 4c). In particular, the changes in thermocline depth highlight the latitudinal differences in the secondary jets' positions (31°N, 35°N, 38°N and 40°N).

The MLD in the two experiments displays a marked seasonal cycle forced by the seasonal cycle of the wind and buoyancy forcing, with a maximum reached in February. Convection down to a depth greater than 1000 m is found in the north of the subpolar gyre (north of 45°*N*, Fig. 4g and h). The shallower winter MLDs are found in the subtropical gyre, except just south of the main jet where MLDs reach ∼200 m), in agreement with existing observations (de Boyer Montégut et al., 2004). In general, the resolution of submesoscale processes results in shallower winter MLDs in B54 in the subpolar gyre, and deeper MLDs in the subtropical gyre (Fig. 4i). These changes are consistent with the changes in isopycnal depth (Fig. 4f).

In summary, submesoscale processes feedback on the large-scale circulation and on the large-scale structure of the thermocline. This feedback is non-local because it involves the displacement and intensification of the mean jet separating the two gyres as well as the formation of alternating zonal jets. Through the thermal wind balance, the density gradients are displaced and strengthened, with global consequences on the thermocline and MLDs.

4.3. Vertical velocity

The statistical properties of the submesoscale features present near the surface in B54 (skewness, slope of velocity spectra) also emphasize that they are strongly associated with frontogenesis processes (Capet et al., 2008; Klein et al., 2008). This implies that the simulated mesoscale turbulence is associated with intense vertical movements in the upper ocean. In both experiments, these vertical movements are particularly intense in the region of the main jets, where eddies are generated (Fig. 6a and b). In B54, the larger number of eddies in the subtropical gyre (south of 30°*N*) leads to larger vertical velocities there. Conversely, in B9 the

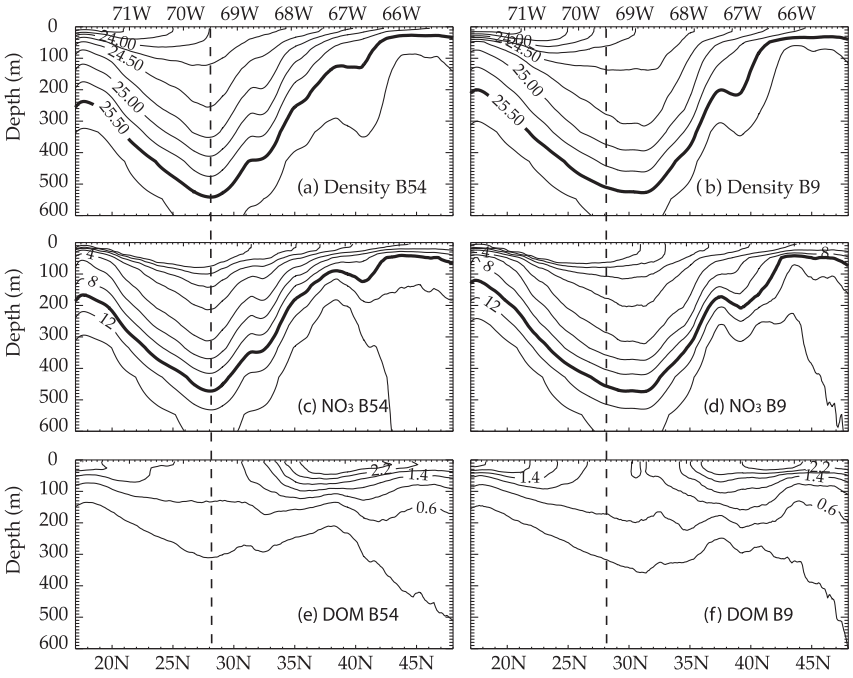

Fig. 5. Vertical section across the domain (indicated on Fig. 4d) of the annual density, nitrate and DOM concentrations for experiments B9 and B54. To facilitate comparison between the two experiments, the dashed line indicates the same position on the left and right panels. The depth of the thermocline (isopycnal 25.5) and nitracline (isonitrate 10 mmol Nm^{-3}) are thickened. Contour intervals are regularly spaced, except for nitrate where contours are 0.1, 0.5 and 1 mmol Nm^{-3} for the three lowest values and are then regularly spaced with a contour interval of 2 mmol Nm^{-3}.

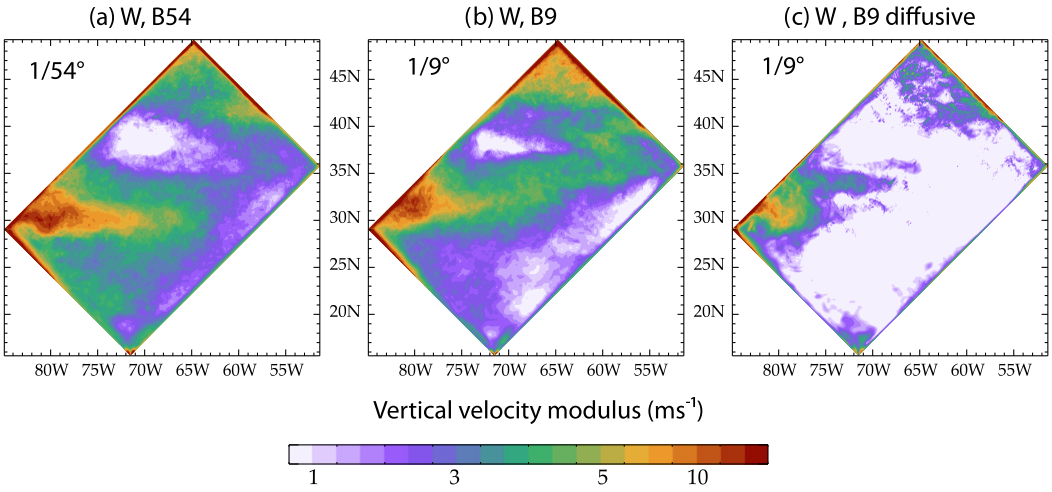

Fig. 6. Annual modulus of the vertical velocity at 120 m depth in experiments B54, B9, and B9-diffusive (see text for more details on the experiments).

northeastward orientation of the main jet leads to larger vertical velocities in the northeast of the domain (Fig. 6b).

Interestingly, the mean magnitude of vertical velocities does not dramatically increase with resolution (order of +30%). This is unlike previous studies, e.g. Lévy et al. (2001b), where a tremendous increase of vertical velocities is found when resolution varies from 6 km to 2 km in a re-entering periodic channel (order of 200%). The strength of vertical velocity increases with increased resolution because of better resolution of submesoscale frontogenesis. The reason why this effect was weak in the present experiments stems from numerical choices. Any change in horizontal resolution must be accompanied by a change in horizontal eddy diffusivity (K_T) and horizontal eddy viscosity (K_M). There is no theory to guide the choice of the turbulent Prandtl number $\left(P_r = \frac{K_M}{K_T}\right)$ for subgrid-scale parameterizations in ocean models. When biharmonic closures are used (as is the case here), some authors have chosen $P_r = 1$ (e.g., Willebrand et al. (2001)). In the quasi-geostrophic regime, the enstrophy cascade is thus simulated in the same manner for the relative vorticity and the vortex stretching components of potential vorticity. Other authors (e.g. Maltrud and McClean (2005)) prefer a Prandlt number larger than unity ($P_r = 3$ in their case). Our choice was to have $P_r = 1$ in B54 and to use the same value of K_T in B54 and in B9, which led to $P_r = 50$ in B9 (Table 1). This choice was guided by an early B9 experiment (experiment B9-diffusive), where we have tested $P_r = 1$ (which implied a larger $K_T = -5 \times 10^{10}\ \mathrm{m}^4 s^{-1}$). This test led to the undesired consequence of a too diffuse thermocline and nutricline (not shown). The comparison of the vertical velocity in B9-diffusive and in B54 gives results in better agreement with the results of Lévy et al. (2001b) (where $P_r = 1$ at all resolutions). The consequence of this choice of a small K_T in B9 is to minimize the differences between B9 and B54 regarding the strength of the eddy driven vertical fluxes. This test on P_r confirms that eddy-resolving experiments (such as B9) are numerically stable over a large set of values for these coefficients and are highly sensitive to them: for example, the dynamics of boundary current separation are known to be critically dependent on eddy parameterisations (Chassignet and Marshall, 2008). A systematic sensitivity analysis is beyond the scope here.

5. Case of sea surface phytoplankton

To illustrate the impacts of submesoscale dynamics, we show how the concentration of phytoplankton at the sea surface varies between B9 and B54, in a daily snapshot (Fig. 3 c and d) and on an annual mean (Fig. 7a and b). Note that there was a marked seasonal cycle of phytoplankton in the model, but there was no noticeable change of this seasonal cycle between the two experiments (not shown). This is why we focus on annual quantities.

Fig. 3c,d shows phytoplankton abundance on March 10, when the bloom is starting at mid-latitudes and concentrations are still low in the northern part of the subpolar gyre. As expected, phytoplankton display significant variability at the submesoscale (see Supplementary material for an animation of this result). Submesoscale patterns in sea surface phytoplankton are present in both experiments and mainly ensue from stirring by the mesoscale flow. Mesoscale stirring distorts the phytoplankton large-scale distribution into filaments of smaller-scale, and is effective in the two experiments because both display an active mesoscale flow (Fig. 3a and b). The impact of horizontal stirring is revealed by the strong connection between phytoplankton distribution and vorticity filaments (Fig. 3). Moreover, in the two experiments, the phytoplankton biomass is generally higher along submesoscale vorticity filaments. This higher biomass is due to more favorable growth conditions there, because of the combined effect of increased stratification and increased supplies of nutrients, as already reported for instance in the studies of Lévy et al. (2001b, 2005). The snapshots illustrate the *local* impact of submesoscale dynamics on phytoplankton, through horizontal stirring, local stratification and local supply of nutrients associated with the process of frontogenesis. The main difference in the small-scale features of phytoplankton distributions between B9 and B54 is related to the presence of small eddies in B54, which are absent in B9, with a clear signature on the phytoplankton distribution.

The annual distribution of sea surface phytoplankton in the model displays significant large-scale contrasts, typical of the sea surface phytoplankton distribution in the North Atlantic and North Pacific (Fig. 7a,b). In both experiments, concentrations are the lowest in the subtropical gyre, and progressively increase toward the north in the subpolar gyre. Sea surface phytoplankton are generally more abundant in B9 than in B54 (Fig. 7c). This result is rather counter-intuitive since mesoscale eddies and submesoscale fronts, which are more energetic in B54, are generally thought to enhance the nutrient supply to the euphotic layer and thus to stimulate phytoplankton growth. The general decrease in phytoplankton abundance between B9 and B54 is most clearly illustrated by the fact that the oligotrophic desert is extending (the area where annual phytoplankton is lower than 0.15 mmol Nm^{-3} increased by 36% in B54) while the bloom area is shrinking (the area where annual phytoplankton is larger than 0.5 mmol Nm^{-3} is decreased by 42% in B54).

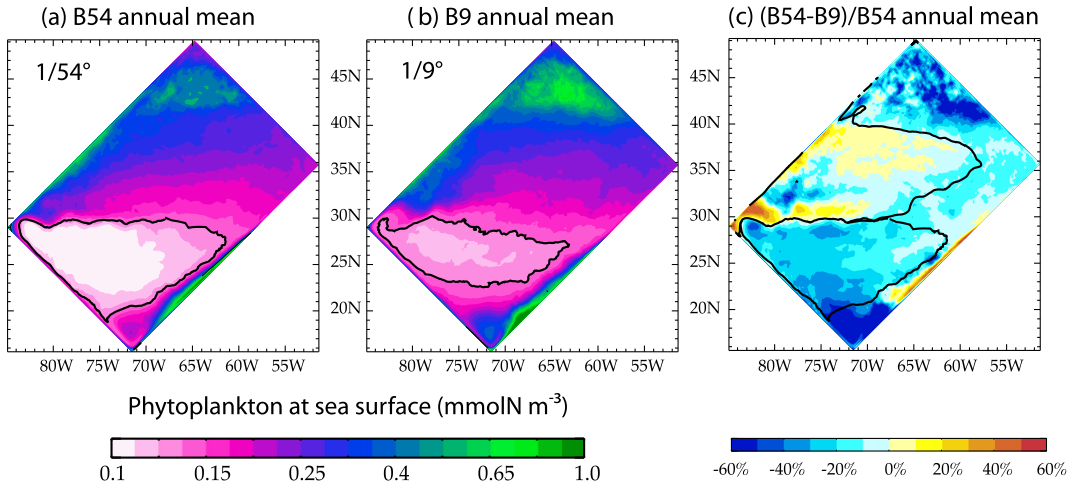

Fig. 7. Annual concentration of phytoplankton at the surface in experiment B54 and B9, and % change between B54 and B9. The black contours on panels (a,b) indicate the 0.15 mmol N/m3 isolignes. The black contours on panel (c) delimit the two provinces defined in Section 5.

In order to understand and quantify those differences, we defined two biogeochemical provinces of interest whose boundaries are shown in Fig. 7c: a "subtropical province" in the oligotrophic subtropical gyre (20–30°N) and a "subpolar province" in the mid-latitude subpolar gyre (30–40°N). To facilitate the comparison between the two experiments, the boundaries of these provinces are fixed in space and time and are identical for B54 and B9. The boundary for the subtropical province is chosen as the 0.15 mmole Nm^{-3} limit of sea surface phytoplankton concentration in B54 (Fig. 7a). The boundary for the subpolar province is chosen as the area in the subpolar gyre where the thermocline depth in B54 is shallower than in B9 by more than 20 m (Fig. 4f). These pragmatic choices enable us to distinguish two fairly different behaviors detailed in the next paragraphs. These two provinces are the most representative of the real ocean. Some other provinces of our configuration will not be further discussed; those include a productive eastern boundary upwelling system between 15–30°N, a deep-convection area north of 40°N and a region of weak southward circulation on the eastern side between 30–40°N. Although these other provinces do also have counter parts in the real ocean, the reduced dimension of our idealized domain and the hypothesis of closed, vertical walls makes their analysis less relevant.

In the subtropical province, sea surface phytoplankton is decreased by 30% between B9 and B54 (Table 4). In the subpolar province, it remains fairly constant on average, although the change is not homogeneous: there are areas where it increases by up to 20–30%, compensated by areas where it decreases (Fig. 7c). In the following, we examine the origin of these differences.

6. Remote biogeochemical impacts of submesoscale dynamics

6.1. Nitrate and DOM

The basin-scale distributions of nitrate and DOM are essential components of the biogeochemical system as they constitute the reservoirs that fuel new and regenerated production of phytoplankton, respectively (DOM being the main source of ammonium in the model). These distributions are examined before a more precise assessment of the change that they induce in terms of phytoplankton productivities (Fig. 8).

The nitrate distribution is controlled by a balance between oceanic circulation and biological activity. In the North Atlantic and North Pacific oceans, the divergence of the horizontal Ekman flux induces upwelling and a raised nitracline in the tropics and subpolar gyre, as well as downwelling and a depressed nitracline in the subtropical gyre, while biological activity maintains a strong vertical gradient. Our model reproduces these main features (Fig. 5c,d). The model nitracline (approximated by the 10 mmol m^{-3} isoline, thick line in Fig. 5c and d) follows very closely the thermocline (thick line in Fig. 5a and b). In fact, in both experiments, the 2D-correlation between nitrate and density taken at the base of the euphotic layer is 0.95. This correlation reaches 0.98 for nitrate and density taken at 300 m. This strong correlation reveals that, in our simulations, the distribution of nitrate at subsurface is controlled by the dynamics, remineralization being of second order. In both experiments, the nitrate content in the euphotic layer is higher at high latitudes, and decreases toward the subtropical gyre (Fig. 8a,b). This structure is due to the deeper MLD in the north, combined with the raised nitracline.

The difference in nitrate reservoir between the two experiments (Fig. 8c) is very similar to the difference in thermocline depth (Fig. 4f). In particular, in the subtropical gyre, there is significantly less nitrate in the euphotic layer in B54 (−63%, Table 4), due to the deepening of the nitracline (Fig. 5c and d). In contrast, there is a tongue of more elevated nitrate concentrations in B54 (+33%, Table 4) between 30–40°N on the western side, which corresponds with the tongue of shallower thermocline in Fig. 4f (i.e. which coincides with the limits of the subpolar province). Note that, as for density, the increased nitrate concentration in this tongue shows zonal patterns associated with the change of position of the series of zonal jets (Fig. 4c).

DOM in the model is the organic matter pool that has the longer residence time. It is produced in the surface layer, essentially by excretion from zooplankton and degradation of detritus. It is produced more abundantly in the north, where phytoplankton productivity is more intense. It is slowly degraded (with a one month time scale) by bacterial activity. This degradation timescale implies that DOM in the model represents the fraction of DOM which is easily degraded, often referred to as semi-labile DOM (Hansell and Carlson, 2002). More labile forms of DOM (with degradation time scales of a few days) are implicitly accounted for in the ammonium compartment, while more refractory forms of DOM (with degradation time scales of more than a few months) are assumed to represent a weak contribution to remineralization and are not accounted for. Consequently, the distribution of DOM in B9 and B54 is characterized by higher concentrations in the

Table 4
Annual mean quantities in the mid-latitude subpolar (30–40°N) and subtropical provinces (20–30°N) delimited in Fig. 7c: new production (NP), regenerated production (RP), total production (PP = NP + RP), nitrification (Nit) and f-ratio (f = NP/PP) within each region. NP, RP, PP and Nit are averaged over the euphotic layer. Vertical mixing, mean advection and eddy advection are the fluxes of nitrate to the euphotic layer. Tot Dyn is the total dynamical supply of nitrate (vertical mixing + mean advection + eddy advection). Results are shown for the experiments B54, B9 and the difference between the two indicated in % is computed as (B54-B9)*100/B54.

	Subpolar			Subtropical			Unit
	B54	B9	B54-B9	B54	B9	B54-B9	
0–5m Phyto	0.25	0.25	−1%	0.11	0.14	−31%	$mmolm^{-3}$
0–120m NO3	410	276	+33%	56	91	−63%	$mmolm^{-2}$
0–120m DOM	175	159	+9%	90	125	−39%	$mmolm^{-2}$
winter MLD	112	154	−42 m	98	82	+16 m	m
NP	1.26	1.31	−4%	0.15	0.19	−25%	$mmolm^{-2}\ d^{-1}$
RP	1.03	1.03	0%	0.43	0.58	−34%	$mmolm^{-2}\ d^{-1}$
PP	2.29	2.34	−2%	0.58	0.77	−32%	$mmolm^{-2}\ d^{-1}$
f-ratio	0.55	0.56		0.26	0.25		
Nit	0.38	0.31	+20%	0.13	0.21	−60%	$mmolm^{-2}\ d^{-1}$
0–120m Phyto	15.8	17.7	−12%	9.2	11.1	−21%	$mmolm^{-2}$
0–120m Zoo	10.0	9.0	+10%	1.2	2.2	−84%	$mmolm^{-2}$
GR	1.32	1.15	+13%	0.10	0.20	−95%	$mmolm^{-2}$
Vertical mixing	0.28	0.52	−84%	0.08	0.08	+4%	$mmolm^{-2}\ d^{-1}$
Mean Advection	0.42	0.09	+78%	−0.10	−0.13	−20%	$mmolm^{-2}\ d^{-1}$
Eddy Advection	0.20	0.36	−81%	0.03	0.03	+14%	$mmolm^{-2}\ d^{-1}$
Tot Dyn	0.90	0.97	−8%	0.01	−0.02	–	$mmolm^{-2}\ d^{-1}$

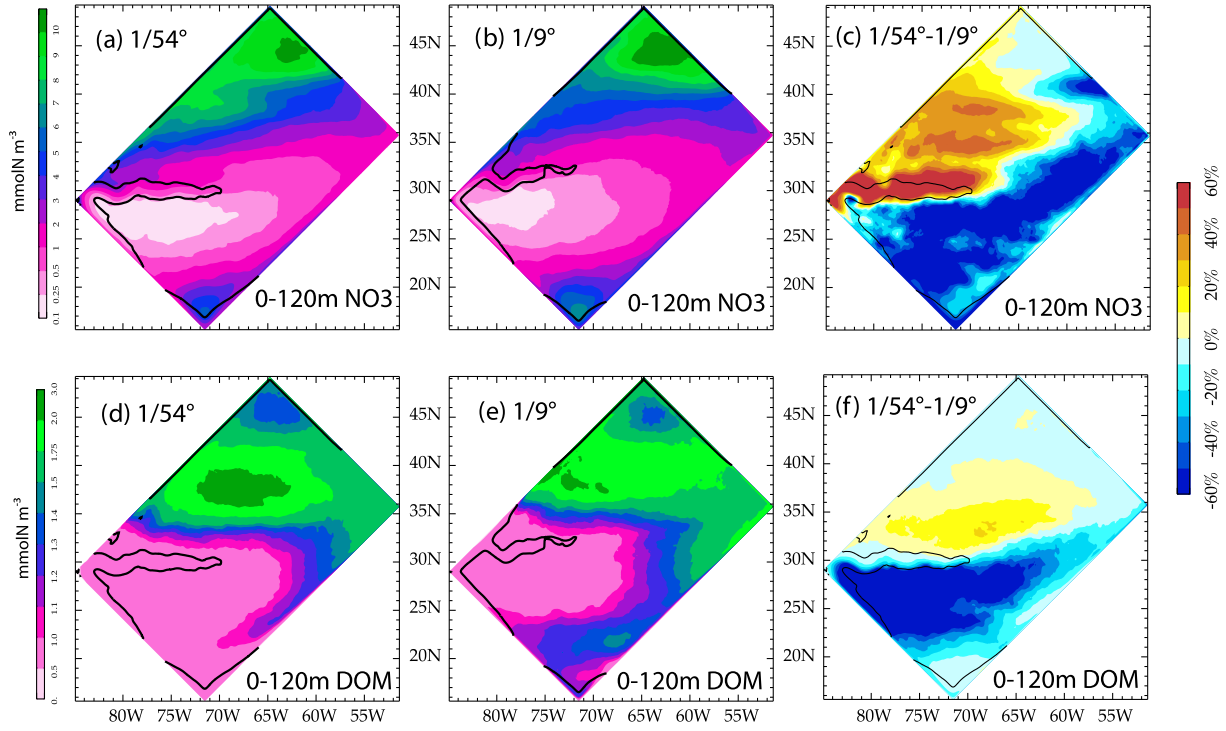

Fig. 8. Annual concentration of nitrate and DOM, averaged over 0–120m, in the experiments B54 and B9, and percent difference between the two (B54-B9/B54). Black contours as in Fig. 4.

north than in the south (Fig. 8d and e), and higher concentrations at the surface, decreasing with depth (Fig. 5e and f). A comparison between experiments (Fig. 8f) displays less DOM in the subtropical province (−39%, Table 4) and more DOM in the subpolar province (+9%, Table 4) in B54. Because of the relatively short residence time of DOM compared to nitrate at subsurface, the DOM distribution is mainly controlled by a balance between biological activity, responsible for the accumulation of DOM at the surface during the productive season, and winter mixing, which exports DOM to depth by dilution when the mixed-layer deepens. This process has been identified in the North Atlantic by Carlson et al. (1994). The pattern of change of DOM (Fig. 8f) resembles the pattern of change of the MLD (Fig. 4i). This strongly suggests that the increased accumulation of DOM in the euphotic layer in the subpolar region in B54 is linked to the shallower MLD (-42 m, Table 4 and reduced dilution, see also Fig. 5f). Conversely, in the subtropical gyre, DOM accumulation is less in B54 because of deeper MLD.

6.2. New and regenerated production

The distinction between nitrate and ammonium in our model allows us to examine separately the phytoplankton production

based on nitrate and on ammonium (new and regenerated production, respectively). The patterns of new and regenerated production are similar in the two model simulations, with high values in the subpolar gyre and low values in the subtropical gyre (Fig. 9a-e). Also, in both experiments, primary production is dominated by new production in the subpolar gyre, while regenerated production exceeds new production in the subtropical gyre (Fig. 9g and h). These general characteristics are observed in the North Atlantic and North Pacific oceans. Interestingly, however, the patterns of change of new and regenerated productions between the two simulations are quite different (Fig. 9c,f). New production is generally larger in B9 than in B54 (by more than 20–40% over large regions), except in the region of the main jet in B54 (−50%) and in a region between 35–40°N on the western side (−20%). Regenerated production is also generally larger in B9 (generally by 10 to 20%), except in a western region roughly located between 30–38°N (−10%). The change in new production (Fig. 9c) results, to first order, from the change in the nitrate reservoir (Fig. 8c): there are two maxima, one at 31°N and the second at 38°N. This general pattern is related to the large scale changes in the position of the jets and the changes in the nitracline depth that they induce. However, in a band between 30–35°N, the nitrate reservoir is larger in B54 (by up to 40%), while new production is larger in B9 (+10 to 20%). This area corresponds to the area where regenerated production is larger in B54 (+10%). We attribute this effect to the inhibition of nitrate uptake in the presence of ammonium (Table 2, Eq. (8)), but a sensitivity test on this parameterization would be necessary to conclude with more certainty. We also note that new production is larger in B54 in the center of the oligotrophic gyre, but this result concerns new production values that are close to zero. On the other hand, the pattern of change in regenerated production (Fig. 9f) is imposed by the change in the DOM reservoir (Fig. 8f). The changes in regenerated production, however, are less than the changes in new production, which dominate the changes in primary production (Fig. 9i).

More quantitatively (Table 4), in the subpolar province, new production is slightly reduced in B54 (−4%) and regenerated production is unchanged. Thus total production and the f-ratio remain relatively unchanged. In the subtropical province, new production is reduced in B54 (−25%) and so is regenerated production (−34%). Thus total production is reduced but the f-ratio remains relatively unchanged (0.26/0.25).

It is noteworthy that in many places in the world's ocean (Yool et al., 2007) as well as in our simulations, a fraction of the nitrate present in the euphotic zone is generated locally through nitrification. In our simulations, changes in nitrification and changes in

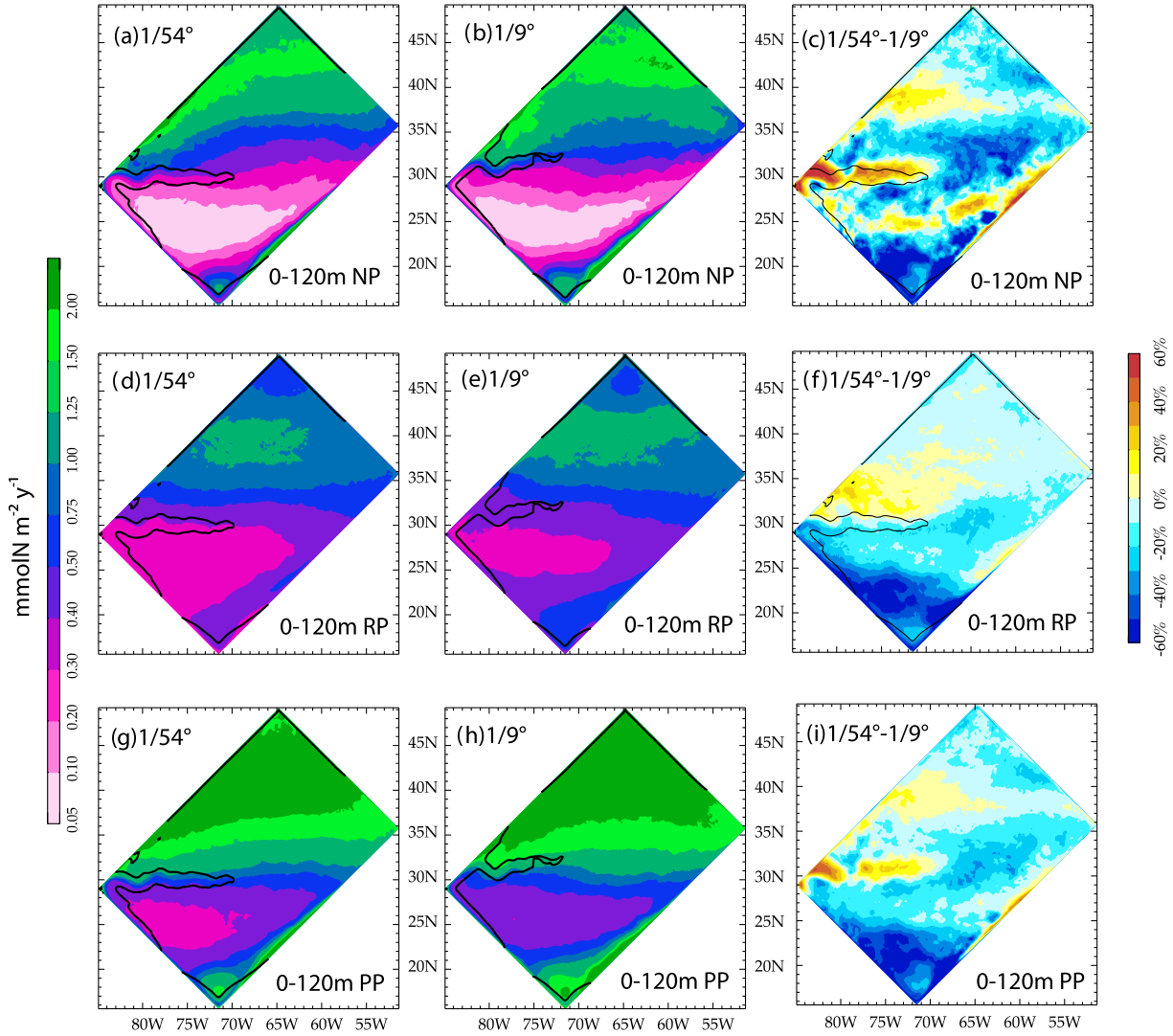

Fig. 9. Annual new production (NP), regenerated production (RP) and primary production (PP = NP + RP) integrated over 0–120m, in the experiments B54 and B9, and difference between the two. The difference is indicated in per cent (B54-B9)/B54. Black contours as in Fig. 4.

regenerated production are similar in pattern (not shown). At higher resolution, nitrification in enhanced in the subpolar region (+20%) and reduced in the subtropical region (−60%).

6.3. Phytoplankton and zooplankton

Finally, phytoplankton and zooplankton abundances in the euphotic layer in B9 and B54, and the change between the two, are shown in Fig. 10. As for sea surface phytoplankton, the main result is that the total phytoplankton biomass in the euphotic layer is reduced in B54, almost everywhere in the domain, from −12% in the subpolar province to −21% in the subtropical province (Fig. 10c and Table 4). Interestingly, the phytoplankton stock is less in B54 even in regions where PP is larger, as for instance in the main jet and between 35–40°N (Fig. 9i). This results from the change in grazing between the experiments (Fig. 10i), and highlights the crucial role of zooplankton in controlling the phytoplankton abundance.

In fact, although the large scale distribution of zooplankton follows the large-scale distribution of phytoplankton, i.e. is characterized by larger values in the subpolar than the subtropical region, the change in zooplankton from B9 to B54 (Fig. 10f) is very different from the change in phytoplankton (Fig. 10c). Zooplankton is more abundant in B54 where nitrate is more abundant (Fig. 8c) and where the mixed-layer is shallower (Fig. 4c). In these areas, the grazing pressure on phytoplankton is enhanced (Fig. 10i), counter balancing the increase of primary production (Fig. 9i).

This result emphasizes that the ecosystem response to the change in circulation and in MLD between B9 and B54 is complex and involves the coupling between phytoplankton and zooplankton: increased nitrate availability in B54 in the subpolar region (between 30–40°N), combined with a shallower mixed-layer, does not lead to an increase of total phytoplankton biomass, as one might have expected, but directly feeds in secondary producers (here, zooplankton). In our experiments, grazing is less efficient when the mixed-layer is deeper. This is particularly true in the subpolar province, where phytoplankton escape their predators more easily in B9 than in B54. This escape does not result from a specific behavior parametrized in the model but is simply the consequence of dilution. This mechanism has been put forward by Marra and Barber (2005) in the North Indian Ocean and by Behrenfeld (2010) in the North Atlantic to explain apparent inconsistency between the change in phytoplankton abundance and phytoplankton growth rates.

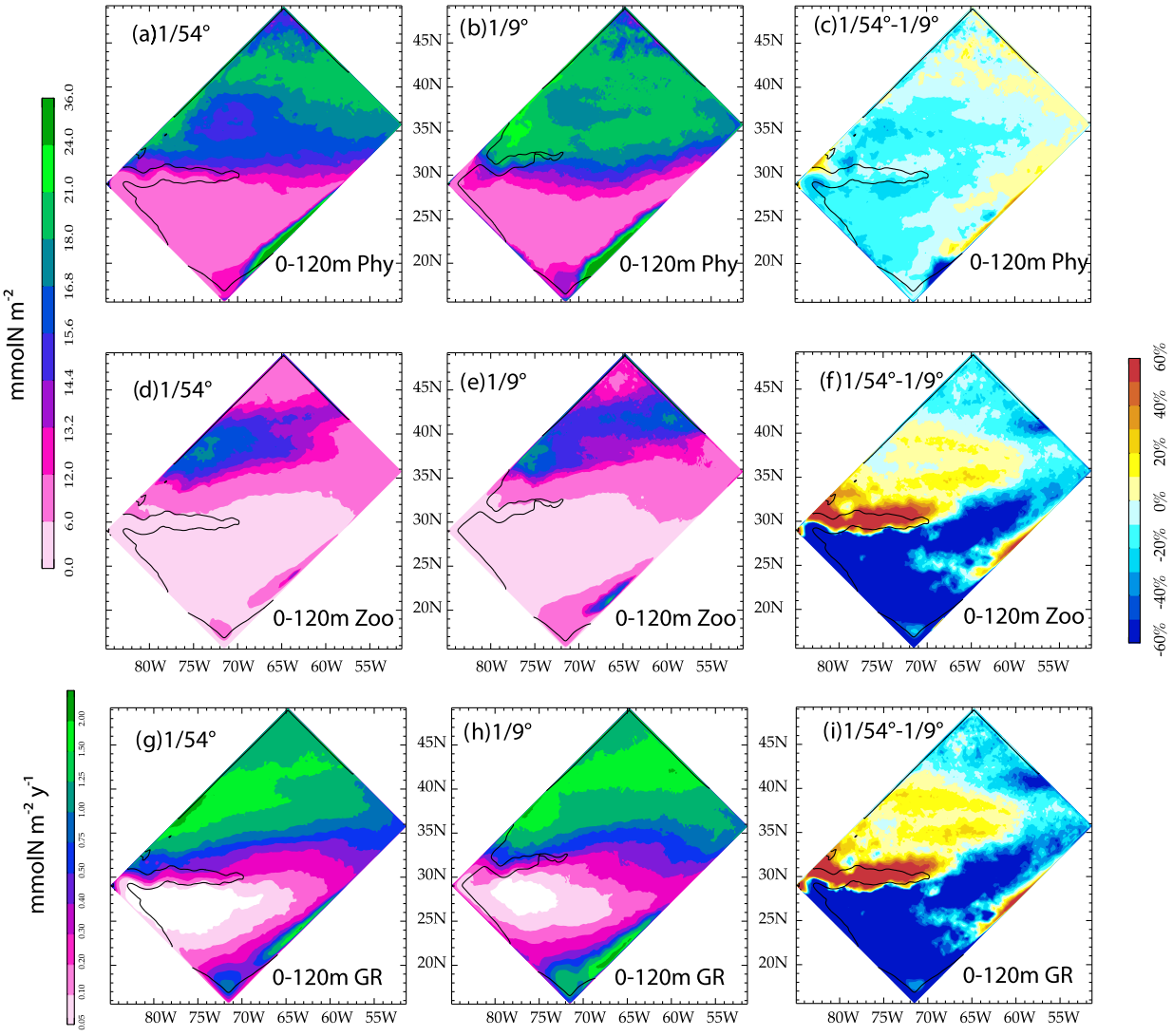

Fig. 10. Annual concentration of phytoplankton (Phy), zooplankton (Zoo) and grazing of phytoplankton by zooplankton (GR), integrated over 0–120m in the experiments B54 and B9, and difference between the two. The difference is indicated in per cent (B54-B9)/B54.

7. Nitrate budget

The two experiments are now compared on the basis of the annual nitrate budget in the euphotic layer. This approach allows us to separate the mean and eddying components of the nitrate advective fluxes via Reynolds decomposition, and to relate the results with previous studies. As seen in the previous sections, increasing the resolution affects both the mean and varying components of the velocity field and of the biogeochemical fields. Thus, it is expected that both the mean and eddy terms in the Reynolds decomposition will vary between B9 and B54. Changes in the mean advection terms can be viewed as the *remote* effects of submesoscale processes, while changes in the eddy terms can be interpreted as the *local* effects of submesoscale processes.

After 50 years of spin-up, the annual concentration of nitrate in the euphotic layer is at equilibrium. This implies that physical transport of nitrate, including advection and vertical mixing, and biological sources and sinks are in balance:

$$\underbrace{-\langle u.\nabla N\rangle}_{\text{advection}}+\underbrace{\left\langle\frac{\partial k_z\partial N}{\partial z^2}\right\rangle}_{\text{vertical mixing}}+\underbrace{\langle S(N)\rangle}_{\text{biological source/sink}}=0 \qquad (1)$$

where the angle brackets denote the average over five years and over the top 120 m, N is the concentration of nitrate, u is the 3D velocity field and k_z is the vertical mixing coefficient. The biological source/sink term S (N) equals new production minus nitrification plus a closure term linked to zooplankton (Eq. (1) in Table 2). This closure term, as well as parametrized biharmonic lateral diffusion, are one order of magnitude smaller and are neglected in this analysis.

Following the Reynolds averaging method, u and N can be decomposed into a mean component ($\bar{u}$ and $\overline{N}$) and a fluctuating eddy component (u' and N' with $\bar{u}'=0$ and $\overline{N}'=0$), which leads to:

$$\underbrace{-\langle\bar{u}.\nabla\overline{N}\rangle}_{\text{mean advection}}\ \underbrace{\overline{-\langle u'.\nabla N'\rangle}}_{\text{eddy advection}}+\underbrace{\overline{\left\langle\frac{\partial k_z\partial N}{\partial z^2}\right\rangle}}_{\text{vertical mixing}}+\underbrace{\overline{\langle S(N)\rangle}}_{\text{biological source/sink}}=0 \qquad (2)$$

The overbar is an operator used to separate the mean from the fluctuating component over a time/spatial scale larger than the mesoscale field. Here, we have chosen a spatial running mean operator over a window of width $\sim$ 200 km (exactly 18 grid points in B9 and 108 in B54) which enables us to keep the seasonal variations in the mean component. However, we have found that using a time-mean operator instead did not change the results (not shown). The operator is not applied at the borders which are excluded from the analysis. Mean advective fluxes are computed as the product of $\bar{u}$ and $\nabla\overline{N}$, which have the temporal resolution of model output (2 days), and are then averaged over 5 years and integrated vertically over 120 m. Total advective fluxes have been archived from the model solution. Eddy advection is computed as the difference between the total advection and the mean advection.

The different terms involved in the physical transport of nitrate to the euphotic layer are compared for the two experiments (Fig. 11 and Table 4). In both experiments, vertical mixing accounts essentially for nutrient entrainment during the winter deepening of the mixed-layer; background diffusion during summer also contributes but is negligible compared to winter mixing. Vertical mixing is the largest in the subpolar gyre, where the winter MLD is the deepest and the nutricline is relatively shallow (Fig. 11a,d). Vertical mixing is larger in B9 than in B54 in a large area between 30–40°N; this is due a to the deeper winter MLD (+42 m, Table 4) that exceeds the change in nitracline depth. In contrast, in the subtropical province, the supply of nitrate by vertical mixing is the same in the two experiments (Table 4), because the deeper nitracline in B54 is balanced by a deeper MLD.

The mean advection pattern (Fig. 11b and e) is imposed by the wind forcing, which forces downward Ekman pumping in the subtropical gyre, and upward pumping in the subpolar gyre. There is also a strong positive contribution of the mean advection along the main jet that acts as a "nutrient stream" (Williams et al., 2006), and which corresponds to the transport of nitrate from the south. Because the jets have different positions in the two experiments (Fig. 4a,b), the areas of maximum mean horizontal advection are also modified, with, in particular, a mean positive advection confined to the western boundary in B9 and penetrating further within the domain and to the north in B54. Thus, in B54 the reduced input of nitrate through vertical mixing in the subpolar province is compensated by larger input through mean advection (Table 4).

Eddy advection (Fig. 11c and f) is negative over the jet area and in the convective region in the north of the subpolar gyre (north of 40°N), but positive in most parts of the subtropical and subpolar provinces. This is consistent with eddies acting to flatten the mean large scale density gradients (Gent and McWilliams, 1990; Gent et al., 1995). There is no tremendous change in eddy advection between the two experiments besides the shift in position of the main patterns, associated with the shift of the mean circulation. In the subpolar province, this shift implies a larger eddy advection in B9 than in B54 (Table 4), in agreement with the tongue of elevated vertical velocity variance which extends toward the northeast in B9 (Fig. 6b). In the subtropical gyre, eddy advection has the same amplitude in B9 and B54: the deeper nitracline in B54 (Fig. 5) is compensated by larger vertical velocities (Fig. 6).

In summary, the changes in the annual nitrate supplies to the euphotic layer stem from a combination of changes in vertical mixing, mean and eddy advection. There are compensations between these different changes. The changes result from changes in nitracline depth, mean circulation, mixed-layer depth and vertical velocity variance. The patterns of eddy advection are shifted in space following the shift of the mean circulation.

Two pioneer studies have estimated the strength of eddy advection of nutrients in the North Atlantic (Oschlies, 2002a; McGillicuddy et al., 2003), with models that had a resolution close to B9. A precise comparison with our results is not straightforward because their two models are realistic of the North Atlantic and ours is an idealized double-gyre and also because their models do not distinguish between nitrate and ammonium, which ours does. Nevertheless, our estimates of eddy advection fall within the range of these studies, even in the case of B54 with higher horizontal resolution. In the northern part of our subpolar gyre (north of 40°N), we found that eddies act to remove nutrients from the euphotic layer, in agreement with the results from these two studies north of 40°N. In the subtropical gyre, McGillicuddy et al. (2003) found that eddy-driven vertical advection of nutrients fuel a significant fraction of the annual new production; on the other hand, Oschlies (2002a) found eddy-driven vertical fluxes of nutrients five times smaller, except near the margins of the gyre, where both vertical and lateral supplies are effective. Our estimates, when considered away from the main jet, are even lower than those of Oschlies (2002a). It is very likely that these differences ensue from the different treatment of nutrient remineralization and equilibration at subsurface. While McGillicuddy et al. (2003) restore subsurface nutrients to climatological values, Oschlies (2002a) solves a unique set of prognostic biological variables both within and below the euphotic zone, and examine the simulation after a spin-up of 3 years, i.e. before complete equilibration of sub-surface nutrient concentrations. Our methodology for the treatment of remineralization is the same as Oschlies (2002a), except that the 50-year spin-up conducted here allows for a much better equilibration. This could explain why our results in the subtropical gyre are more consistent with the results of Oschlies (2002a) than with the

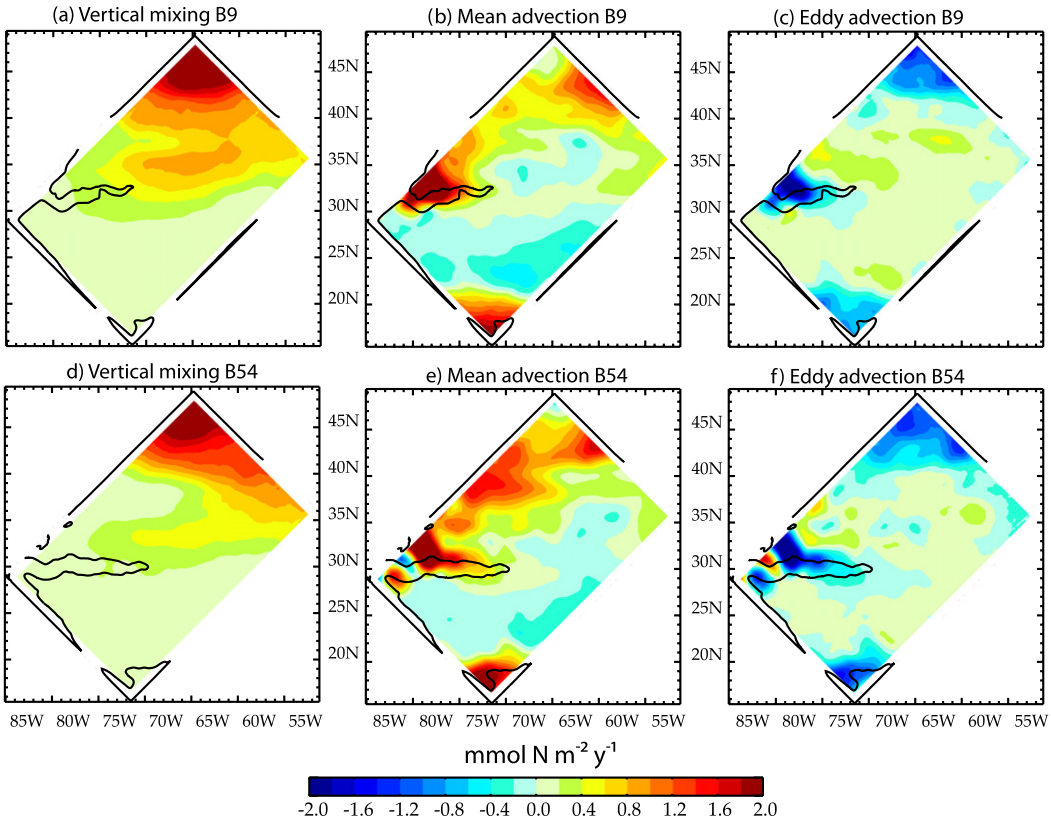

Fig. 11. Annual dynamical nitrate supplies in the upper 120 m, comprising vertical mixing and advection. Advective fluxes are separated into their mean and eddying components (see text).

results of McGillicuddy et al. (2003), although it should be noted that nutrient supplies and primary production in our model's subtropical gyre is in the lower range of what is simulated in the two above models as well as in observations in the North Atlantic (Oschlies, 2002b). This comparison highlights the crucial role of the long-term equilibration of the system to get a fully consistent picture. The long-term equilibration leads to differences which are at least as important as a change in horizontal resolution. It impacts the eddy advective fluxes as well as the mean fluxes.

8. Concluding discussion

In this paper we have analyzed long (50 years) integrations of an idealized double-gyre circulation at mesoscale and submesoscale resolving resolutions ((1/9)° and (1/54)°) that allow us to demonstrate the *remote*, large-scale feedbacks of submesoscale dynamics on a fully-conserving ecosystem. Our configuration is characteristic of the bloom and oligotrophic regimes in mid-latitudes oceanic gyres, such as the Gulf Stream system in the North Atlantic or the Kuroshio system in the North Pacific. When horizontal resolution is increased from eddy-resolving to submesoscale resolving, a strongly turbulent eddy field emerges that significantly and globally modifies the model mean fields. Our (1/54)° resolution simulation is characterized by a current separating the two gyres that is more zonal and shifted to the south; the MLD and nitracline are deeper in the subtropical gyre and shallower over large parts of the subpolar gyre than in our (1/9)° simulation.

Our idealized experiments display, quite unexpectedly, a decrease in the phytoplankton abundance as the resolution is refined. This decrease is the signature that the biogeochemical system has not reached the same equilibrium in the two simulations. In order to understand the origin of the difference, we related the changes of the ecosystem to those of the physical forcing. Understanding the differences between two different biogeochemical equilibria is not straightforward since the mean biogeochemical concentrations result from the balance of equations to which all terms contribute. Nevertheless, the following, simplified scheme emerged from our analysis (Table 4).

In the subtropical gyre, the decrease in phytoplankton abundance (∼−20%) at higher resolution is accompanied by a decrease in zooplankton abundance (∼−80%). It ensues primarily from the decrease in primary production (from 0.77 to 0.58 mmoleN $m^{-2}d^{-1}$) which exceeds the decrease in grazing (from 0.20 to 0.10 mmoleN $m^{-2}d^{-1}$). The deepening of the nitracline does not imply less nitrate supplies because it is accompanied by a concomitant deepening of the winter MLD. The decrease in primary production results in fact from the decrease of regeneration (∼-34%). The origin of this decrease is mediated by the more efficient export of DOM by vertical mixing during winter (due to the deeper winter MLD). It is then reinforced by a positive feedback, since less primary production implies less total living biomass (phytoplankton plus zooplankton) and thus less local regeneration.

At mid-latitudes in the subpolar gyre (Table 4), the changes involve a modification of the interactions between trophic levels in the ecosystem: the decrease in phytoplankton abundance (∼−10%) is associated with an increase in zooplankton abundance (+10%). In contrast to the case of the subtropical gyre, the shallower mixed-layer at higher resolution implies a better retention of DOM, leading to higher nitrification (+20%). It also leads to a strong reduction of convective nitrate inputs, partly balanced by advection. These two effects balance each other such that the total primary production is approximately the same. At the same time, the shallower mixed-layer also implies more efficient grazing,

which ultimately causes the increase in zooplankton abundance and the decrease in phytoplankton abundance.

Thus the changes in MLD and nutricline depth appear to be at the origin of the different equilibria for the two simulations. The deeper MLD and nutricline in B54 (case of the subtropical gyre) are associated with less DOM, less regeneration and less zooplankton. This leads to a decrease in phytoplankton abundance because of reduced primary production. The shallower MLD and nutricline (case of the subpolar gyre) are conversely associated with more DOM, more regeneration and more zooplankton. This also leads to a decrease in phytoplankton abundance, but this time because of increased grazing. The changes in DOM and zooplankton in response to the change in MLD ensue from different reasons: changes in dilution in the case of DOM and changes in the coupling between phytoplankton and zooplankton (also mediated by dilution effects) in the case of zooplankton. But they are also linked by a positive feedback, since more zooplankton produce more DOM. It should be noted that the exact values of % changes between experiments computed in Table 4 depend on the criteria used for the choice of the province boundaries. Sensitivities to these criteria have revealed that the conclusions are robust.

Regarding the physical transport of nutrients within the euphotic layer, our results provide a complementary view with regards to previous studies. While many of the previous studies, based on short-term perturbation experiments (e.g. Lévy et al. (2001b)), have shown that the strength of the eddy transport of nutrients strongly depends on resolution, here we show that the large-scale distribution of the eddy transport is linked to the changes of the model mean state with resolution. Moreover, we highlight important changes in the supplies by the mean circulation and by vertical mixing which are also consequences of the change in resolution. The repercussion is that increasing the model resolution does not necessarily increase the supplies of nutrients at mid-latitudes, as suggested by earlier studies, when the model is integrated long enough to account for the *remote* impacts of submesoscale processes.

Our experiments are idealized in many ways, which makes it difficult to anticipate the changes implied by submesoscale resolution in a more realistic setting. Moreover, we should note that the idealized nature of the experiments does not permit direct comparison with observations in the North Atlantic or North Pacific; this prevents stating which experiment is the most valid from an observational perspective. Nevertheless, our results illustrate that increasing a model resolution from eddy-resolving to submesoscale-resolving has both *remote* and *local* impacts on the ecosystem. The large changes in the mean state that we obtained could be amplified by our choice of a flat-bottom basin: in the real ocean the mean flow is strongly constrained by the bathymetry. These large changes make it difficult to compare the model runs in a more quantitative way. Moreover, the moderate changes in the strength of the eddy fluxes reported here are probably a lower bound. Those might be increased with a different choice of eddy diffusivity coefficients. Also, we did not account for high-frequency wind events, which are known to feedback positively on the strength of vertical velocity in sub-mesoscale filaments (Lévy et al., 2009; Danioux et al., 2011); this effect might also increase the differences in vertical eddy fluxes between the two experiments. Future work should also address the role of the biodiversity of primary producers, in connection with export and grazing, as well as the role played by the quality of the DOM. Nonetheless, with the present idealized model, and within the chosen set of model parameters, submesoscale processes modify the biogeochemical equilibria through *remote* impacts more radically than through *local* impacts. Particularly, the main result of a decreased phytoplankton abundance at higher resolution ensues from these *remote* effects, whereas the *local* effects have been previously shown to tend to increase the phytoplankton stock only before complete equilibration of the system.

Acknowledgements

The project was supported by CNRS (INSU-LEFE TWISTED project), ANR (INLOES project) and MERCATOR (Multicolor project). This work is a contribution to the Memorandum of Understanding (MOU) between the Earth Simulator Center, CNRS and IFREMER. The spin-up was performed on the Earth simulator (ESC, Yokohama, Japan), and the five-year runs at IDRIS (France). This manuscript was improved thanks to the very helpful comments of two anonymous reviewers, of the associate editor A. Oschlies, of L. Memery and A. Martin. M.A. Foujols is thanked for developing the code on the Earth Simulator, and C. Ethé for running it at IDRIS. Many thanks to R. Benshila, C. Talandier, F. Pinsard, P. Brockmann, A. Caubel, E. Maisonneuve, C. Deltel, C. Ethé. M. Kolasinski, S. Denvil, J. Ghattas and P. Brochard who have come to the ESC to run the simulations. Their visits at the ESC were greatly facilitated by the kind help of A. Kurita, R. Itakura, A. Toya and M.-E. Demory.

Appendix A. Supplementary data

Supplementary data associated with this article can be found, in the online version, at doi:10.1016/j.ocemod.2011.12.003.

References

Allen, J., Brown, L., Sanders, R., Moore, C., Mustard, A., Fielding, S., Lucas, M., Rixen, M., Savidge, G., Henson, S., 2005. Diatom carbon export enhanced by silicate upwelling in the northeast atlantic. Nature 437, 728–732.

Allen, J., Smeed, D., Nurser, A., Zhang, J., Rixen, M., 2001. Diagnosis of vertical velocities with the qg omega equation: an examination of the errors due to sampling strategy. Deep Sea Res. Part I: Oceanogr. Res. Papers 48, 315–346.

Barnier, B., Hua, L.B., LeProvost, C., 1991. On the catalytic role of high baroclinic modes in eddy driven large scale circulations. J. Phys. Ocean 21, 976–997.

Behrenfeld, M., 2010. Abandoning sverdrup's critical depth hypothesis on phytoplankton blooms. Ecology 91, 977–989.

Blanke, B., Delecluse, P., 1993. Variability of the tropical atlantic ocean simulated by a general circulation model with two different mixed-layer physics. J. Phys. Oceanogr. 23, 1363–1388.

de Boyer Montégut, C., Madec, G., Fischer, A., Lazar, A., Iudicone, D., 2004. Mixed layer depth over the global ocean: an examination of profile data and a profile-based climatology. J. Geophys. Res. 109, C12003.

Calil, P.H.R., Richards, K.J., 2010. Transient upwelling hot spots in the oligotrophic north pacific. J. Geophys. Res. 115, C02003.

Capet, X., McWilliams, J., Molemaker, M., Shchepetkin, A., 2008. Mesoscale to submesoscale transition in the california current system. Part I: Flow structure, eddy flux, and observational tests. J. Phys. Oceanogr. 38, 29–43.

Carlson, C., Ducklow, H., Michaels, A., 1994. Annual flux of dissolved organic carbon from the euphotic zone in the northwest sargasso sea. Nature 371, 405–408.

Chassignet, E., Marshall, D.P., 2008. Gulf Stream separation in numerical ocean models. In: Eddy resolving ocean modelling, M. Hecht, H. Hasumi, Eds., AGU Monograph Series, pp. 39–62.

Danioux, E., Klein, P., Hecht, M., Komori, N., Roullet, G., LeGentil, S., Sasaki, H., 2011. Emergence of wind-driven near-inertial waves in the deep ocean triggered by small-scale eddy vorticity structures. J. Phys. Oceanogr. 41, 1297–1307.

d'Ovidio, F., Isern-Fontanet, J., López, C., Hernández-García, E., Garcia-Ladona, E., 2009. Comparison between eulerian diagnostics and finite-size lyapunov exponents computed from altimetry in the algerian basin. Deep Sea Res. Part I: Oceanogr. Res. Papers 56, 15–31.

Drijfhout, S., 1994. On the heat transport by mesoscale eddies in an ocean circulation model. J. Phys. Oceanogr. 24, 429–442.

Feldmann, G.C. et al., 1989. Ocean color: availability of the global data set. EOS Trans. AGU 70, 640–641.

Gent, P.R., McWilliams, J.C., 1990. Isopycnal mixing in ocean circulation models. J. Phys. Oceanogr. 20, 150–155.

Gent, P.R., Willebrand, J., McDougall, T.J., McWilliams, J.C., 1995. Parameterizing eddy-induced tracer transports in ocean circulation models. J. Phys. Oceanogr 25, 463–474.

Gower, J., Denman, K., Holyer, R., 1980. Phytoplankton patchiness indicates the fluctuation spectrum of mesoscale oceanic structure. Nature 288, 157.

Hansell, D., Carlson, C., 2002. Biogeochemistry of marine dissolved organic matter. Academic Press, San Diego.

Haza, A., Poje, A., Özgökmen, T., Martin, P., 2008. Relative dispersion from a high-resolution coastal model of the adriatic sea. Ocean Model. 22, 48–65.

Hazeleger, W., Drijfhout, S., 1999. Stochastically forced mode water variability. J. Phys. Oceanogr. 29, 1772–1786.
Hazeleger, W., Drijfhout, S., 2000a. Eddy subduction in a model of the subtropical gyre. J. Phys. Oceanogr. 30, 677–695.
Hazeleger, W., Drijfhout, S., 2000b. A model study on internally generated variability in subtropical mode water formation. J. Geophys. Res. 105, 13.
Hazeleger, W., Drijfhout, S., Netherl, R., Bilt. . ., D., 1996. Mode water variability in a model of the subtropical gyre: response to anomalous forcing. J. Phys. Oceanogr. 28, 266–288.
Hurlburt, H., Hogan, P., 2000. Impact of 1/8 to 1/64 resolution on gulf stream model-data comparisons in basin-scale subtropical atlantic ocean models. Dyn. Atmos. Oceans 32, 283–329.
Johnson, K.S., Riser, S.C., Karl, D.M., 2010. Nitrate supply from deep to near-surface waters of the north pacific subtropical gyre. Nature 465, 1062–1065.
Kamenkovich, I., Berloff, P., Pedlosky, J., 2009. Role of eddy forcing in the dynamics of multiple zonal jets in a model of the north atlantic. J. Phys. Oceanogr. 39, 1361–1379.
Karleskind, P., Lévy, M., Mémery, L., 2011a. Modifications of mode water properties by sub-mesoscales in a bio-physical model of the northeast atlantic. Ocean Model. 39, 47–60.
Karleskind, P., Lévy, M., Memery, L., 2011b. Subduction of carbon, nitrogen, and oxygen in the northeast atlantic. J. Geophys. Res. 116, C02025.
Klein, P., Hua, B., Lapeyre, G., Capet, X., Gentil, S.L., Sasaki, H.S., 2008. Upper ocean turbulence from high 3-d resolution simulations. J. Phys. Oceanogr. 38, 1748–1763.
Klein, P., Lapeyre, G., 2009. The oceanic vertical pump induced by mesoscale and submesoscale turbulence. Ann. Rev. Marine Sci. 1, 351–375.
Krémeur, A., Lévy, M., Aumont, O., Reverdin, G., 2009. Impact of the subtropical mode water biogeochemical properties on primary production in the north atlantic: New insights from an idealized model study. J. Geophys. Res. 114, C07019.
Lathuilière, C., Echevin, V., Lévy, M., Madec, G., 2010. On the role of the mesoscale circulation on an idealized coastal upwelling ecosystem. J. Geophys. Res. 115, C09018.
Lathuiliere, C., Lévy, M., Echevin, V., 2011. Impact of eddy-driven vertical fluxes on phytoplankton abundance in the euphotic layer. J. Plank. Res. 33, 5, 827–83.
Le-Galloudec, O., Bourdalle-Badie, R., Drillet, Y., Derval, C., Bricaud, C., 2008. Simulation of meso-scale eddies in the mercator global ocean high resolution model. Mercator Newsletter, 31.
Lee, M., Williams, R., 2000. The role of eddies in the isopycnic transfer of nutrients and their impact on biological production. J. Mar. Res. 58, 895–917.
Lehahn, Y., d'Ovidio, F., Lévy, M., Heifetz, E., 2007. Stirring of the northeast atlantic spring bloom: A lagrangian analysis based on multisatellite data. J. Geophys. Res. 112, C08005.
LeSommer, J., d'Ovidio, F., Madec, G., 2011. Parameterization of subgrid stirring in eddy resolving ocean models. part 1: Theory and diagnostics. Ocean Model. 39, 154–169.
Lévy, M., 2008. The modulation of biological production by oceanic mesoscale turbulence. In: Weiss, J.B., Provenzale, A. (Eds.), Transport in Geophysical Flow: Ten years after. Springer, pp. 219–261.
Lévy, M., Estubier, A., Madec, G., 2001a. Choice of an advection scheme for biogeochemical models. Geophys. Res. Lett. 28, 3725–3728.
Lévy, M., Gavart, M., Mémery, L., Caniaux, G., Paci, A., 2005. A four-dimensional mesoscale map of the spring bloom in the northeast atlantic (pomme experiment): Results of a prognostic model. J. Geophys. Res, 110.
Lévy, M., Klein, P., 2004. Does the low frequency variability of mesoscale dynamics explain a part of the phytoplankton and zooplankton spectral variability? Proc. Roy. Soc. Lon A 460, 1673.
Lévy, M., Klein, P., Jelloul, M.B., 2009. New production stimulated by high-frequency winds in a turbulent mesoscale eddy field. Geophys. Res. Lett. 36, 1–5.
Lévy, M., Klein, P., Treguier, A., 2001b. Impacts of sub-mesoscale physics on phytoplankton production and subduction. J. Mar. Res. 59:4, 535–565.
Lévy, M., Klein, P., Tréguier, A., Iovino, D., Madec, G., Masson, S., Takahashi, K., 2010. Modifications of gyre circulation by sub-mesoscale physics. Ocean Model., 34.
Lévy, M., Memery, L., Madec, G., 1998. The onset of a bloom after deep winter convection in the northwestern mediterranean sea: mesoscale process study with a primitive equation model. J. Marine Syst. 16, 7–21.
Madec, G., 2008. Nemo ocean engine. Note du Pole de modelisation de l'Institut Pierre-Simon Laplace 27, 1–217.
Mahadevan, A., Tandon, A., 2006. An analysis of mechanisms for submesoscale vertical motion at ocean fronts. Ocean Model. 14 (3-4), 241–256.
Maltrud, M., McClean, J., 2005. An eddy resolving global 1/10° ocean simulation. Ocean Model. 8, 31–54.
Marra, J., Barber, R.T., 2005. Primary productivity in the arabian sea: a synthesis of jgofs data. Progr. Oceanogr. 65, 159–175.
Martin, A., Pondaven, P., 2003. On estimates for the vertical nitrate flux due to eddy pumping. J. Geophys. Res. 108 (C11), 3359.
Martin, A., Richards, K., Fasham, M., 2001. Phytoplankton production and community structure in an unstable frontal region. J. Marine Syst. 28, 65–89.
Maximenko, N., Bang, B., Sasaki, H., 2005. Observational evidence of alternating zonal jets in the world ocean. Geophys. Res. Lett 32, L12607.
McGillicuddy, D., Anderson, L., Bates, N., Bibby, T., Buesseler, K., Carlson, C., Davis, C., Ewart, C., Falkowski, P., Goldthwait, S., Hansell, D., Jenkins, W., Johnson, R., Kosnyrev, V., Ledwell, J., Li, Q., Siegel, D., Steinberg, D., 2007. Eddy/wind interactions stimulate extraordinary mid-ocean plankton blooms. Science 316, 1021–1026.
McGillicuddy, D., Anderson, L., Doney, S., Maltrud, M., 2003. Eddy-driven sources and sinks of nutrients in the upper ocean: Results from a 0.1° resolution model of the north atlantic. Global Biogeochem. Cycles 17 (2), 1035.
McWilliams, J.C., 1984. The emergence of isolated coherent vortices in turbulent flow. J. Fluid Mech. 146, 21–43.
Memery, L., Arhan, M., Alvarez-Salgado, X.A., Messias, M.J., Mercier, H., Castro, C.G., Rios, A.F., 2000. The water masses along the western boundary of the south and equatorial atlantic. Progr. Oceanogr. 47, 69–98.
Nagai, T., Tandon, A., Gruber, N., McWilliams, J., 2008. Biological and physical impacts of ageostrophic frontal circulations driven by confluent flow and vertical mixing. Dyn. Atmos. Oceans 45, 229–251.
Nakamura, M., Kagimoto, T., 2006. Potential vorticity and eddy potential enstrophy in the north atlantic ocean simulated by a global eddy-resolving model. Dyn. Atmos. Oceans 41, 28–59.
Omta, A., Kooijman, B., Dijkstra, H., 2007. Influence of (sub) mesoscale eddies on the soft-tissue carbon pump. J. Geophys. Res. 112, C11009.
Oschlies, A., 2002a. Can eddies make ocean deserts bloom. Global Biogeochem. Cycles 16, 1106.
Oschlies, A., 2002b. Nutrient supply to the surface waters of the north atlantic: A model study. J. Geophys. Res. 107, 1–14.
Perruche, C., Rivière, P., Lapeyre, G., XCarton, Pondaven, P., 2011. Effects of surface quasi-geostrophic turbulence on phytoplankton competition and coexistence. J. Mar. Res. 69, 105–135.
Pollard, R., Regier, L., 1990. Large variations in potential vorticity at small spatial scales in the upper ocean. Nature 348, 227–229.
Provenzale, A., 1999. Transport by coherent barotropic vortices. Ann. Rev. Fluid Mech. 31, 55–93.
Rivière, P., Pondaven, P., 2006. Phytoplankton size classes competitions at sub-mesoscale in a frontal oceanic region. J. Marine Syst..
Sasaki, Y., Minobe, S., Schneider, N., Kagimoto, T., Nonaka, M., Sasaki, H., 2008. Decadal sea level variability in the south pacific in a global eddy-resolving ocean model hindcast. J. Phys. Oceanogr. 38, 1731–1747.
Siegel, A., Weiss, J., Toomre, J., McWilliams, J., Berloff, P., Yavneh, I., 2001. Eddies and vortices in ocean basin dynamics. Geophys. Res. Lett. 28, 3183–3186.
Thomas, L., Ferrari, R., 2008. Friction, frontogenesis, and the stratification of the surface mixed layer. J. Phys. Oceanogr. 38, 2501–2518.
Thomas, L.N., Lee, C.M., Yoshikawa, Y., 2010. The subpolar front of the japan/east sea. part ii: Inverse method for determining the frontal vertical circulation. J. Phys. Oceanogr. 40, 3.
Thomas, L.N., Tandon, A., Mahadevan, A., 2007. Submesoscale processes and dynamics. AGU Monograph on Eddy Resolving Ocean Model., 1–15.
Viúdez, Á., Claret, M., 2009. Numerical simulations of submesoscale balanced vertical velocity forcing unsteady nutrient phytoplankton zooplankton distributions. J. Geophys. Res. 114, C04023.
Waugh, D.W., Abraham, E.R., 2008. Stirring in the global surface ocean. Geophys. Res. Lett. 35, L20605.
Willebrand, J., Barnier, B., Boning, C., Dieterich, C., Killworth, P., Provost, C.L., Jia, Y., Molines, J., New, A., 2001. Circulation characteristics in three eddy-permitting models of the north atlantic. Progr. Oceanogr. 48, 123–161.
Williams, R., Follows, M., 1998. The ekman transfer of nutrients and maintenance of new production over the north atlantic. DSRI 45, 461–490.
Williams, R., Roussenov, V., Follows, M., 2006. Nutrient streams and their induction into the mixed layer. Global Biogeochem. Cycles, 20.
Yool, A., Martin, A., Fernández, C., Clark, D., 2007. The significance of nitrification for oceanic new production. Nature 447, 999–1002.